

May 6, 2020

Global alignment and assessment of TRP channel transmembrane domain structures to explore functional mechanisms

Katherine E. Huffer¹, Antoniya A. Aleksandrova², Andrés Jara-Oseguera¹, Lucy R. Forrest² and Kenton J. Swartz¹

- 1 Molecular Physiology and Biophysics Section, Porter Neuroscience Research Center, National Institute of Neurological Diseases and Stroke, National Institutes of Health, Bethesda, MD 20892.
- 2 Computational Structural Biology Section, Porter Neuroscience Research Center, National Institute of Neurological Diseases and Stroke, National Institutes of Health, Bethesda, MD 20892.

Correspondence to: Kenton.Swartz@nih.gov

Abstract

The recent proliferation of published TRP channel structures provides a foundation for understanding the diverse functional properties of this important family of ion channel proteins. To facilitate mechanistic investigations, we constructed a structure-based alignment of the transmembrane domains of 120 TRP channel structures. Comparison of structures determined in the absence or presence of activating stimuli reveals similar constrictions in the central ion permeation pathway near the intracellular end of the S6 helices, pointing to a conserved cytoplasmic gate and suggesting that most available structures represent non-conducting states. Comparison of the ion selectivity filters towards the extracellular end of the pore supports existing hypotheses for mechanisms of ion selectivity. Also conserved to varying extents are hot spots for interactions with hydrophobic ligands, lipids and ions, as well as discrete alterations in helix conformations. This analysis therefore provides a framework for investigating the structural basis of TRP channel gating mechanisms and pharmacology, and, despite the large number of structures included, reveals the need for additional structural data and for more functional studies to establish the mechanistic basis of TRP channel function.

Introduction

Transient Receptor Potential (TRP) channels are a large and diverse family of cation permeable ion channel proteins that are expressed in animals and yeast, algae and other unicellular organisms. The biological functions of TRP channels are remarkably diverse, and include nociception, thermosensation, immune cell function, control of cellular excitability, fluid secretion, cardiac and smooth muscle function and development, ion homeostasis and lysosomal function (Nilius and Flockerzi, 2014; Ramsey et al., 2006; Venkatachalam and Montell, 2007). The family name is derived from the drosophila mutant that causes blindness in which the neurons of mutant flies exhibit a transient receptor potential (trp) instead of a persistent response to illumination with intense light in electroretinograms (Cosens and Manning, 1969). The trp mutation was subsequently localized to the protein that functions as the phototransduction channel in the drosophila retina (Montell, 2011). TRP channels have been classified into seven subfamilies: TRPC (canonical), TRPV (vanilloid), TRPM (melastatin), TRPA (ankyrin), TRPN (NOMPC), TRPP (polycystic) and TRPML (mucolipin) (Clapham, 2007). As expected from their widespread expression and physiological roles, mutations in TRP channels cause a range of human diseases and are considered important drug targets for pain, inflammation, asthma, cancer, anxiety, cardiac disease and metabolic disorders (Moran, 2018; Nilius et al., 2007).

TRP channels have a notable historical significance in membrane protein structural biology because the structure of TRPV1 determined in 2013 ushered in a new era for solving near-atomic resolution structures of membrane proteins using cryo-electron microscopy (cryo-EM) (Cao et al., 2013; Liao et al., 2013). At least one structure has now been reported for each subfamily, with a total of 136 TRP channel structures available (Autzen et al., 2018; Cao et al., 2013; Chen et al., 2017; Dang et al., 2019; Deng et al., 2018; Diver et al., 2019; Dosey et al., 2019; Duan et al., 2019; Duan et al., 2018b; Duan et al., 2018c; Fan et al., 2018; Grieben et al., 2017; Guo et al., 2017; Hirschi et al., 2017; Huang et al., 2018; Hughes et al., 2019; Hughes et al., 2018a; Hughes et al., 2018b; Hulse et al., 2018; Huynh et al., 2016; Jin et al., 2017; Liao et al., 2013; McGoldrick et al., 2019; McGoldrick et al., 2018; Paulsen et al., 2015; Saotome et al., 2016; Shen et al., 2016; Singh et al., 2019; Singh et al., 2018a; Singh et al., 2018b; Singh et al., 2018c; Su et al., 2018a; Su et al., 2018b; Tang et al., 2018; Vinayagam et al., 2018; Wang et al., 2018; Wilkes

et al., 2017; Winkler et al., 2017; Yin et al., 2019a; Yin et al., 2019b; Yin et al., 2018; Zhang et al., 2018a; Zheng et al., 2018; Zhou et al., 2017; Zubcevic et al., 2019a; Zubcevic et al., 2016; Zubcevic et al., 2018a; Zubcevic et al., 2018b). These structures show that TRP channels are tetramers, with each subunit containing six transmembrane (TM) helices (S1-S6), and with the S5 and S6 helices from the four subunits forming a central pore domain containing the ion permeation pathway (Figures 1 and 3). The S1-S4 helices form peripheral domains within the membrane with a domain-swapped architecture such that each S1-S4 domain is positioned near to the pore-forming S5-S6 helices from the adjacent subunit (Figure 1A,B). The N- and C-termini contribute to forming large intracellular domains that differ extensively between subfamilies (Figure 1F-M). Most TRP channels also contain a highly conserved helical extension of the pore-lining S6 helix named the TRP box that projects through a tunnel formed by the intracellular-facing surface of the S1-S4 domain and the pre-S1 region of the N-terminus (Figure 1F,I-M). In many instances, structures of the same TRP channel have been determined in the absence and presence of activating ligands and toxins, inhibitors, or with mutations that promote open or closed states, providing a wealth of information about the structural basis of their functional properties and pharmacology.

To synthesize what has been learned from these TRP channel structures, and to provide a framework for comparing structural elements in functionally critical regions, we generated a structure-based alignment of the transmembrane domains for most of the available TRP channel structures. We used the structural alignment to compare key regions of the ion permeation pathways in the context of their roles in ion selectivity and gating, as well as binding sites for ligands and regulatory ions. Remarkably, even though our analysis considers an unprecedented number of related ion channel structures, it identified the need for additional structural data and for more functional studies to establish the mechanistic basis of TRP channel function and pharmacology.

Results

Structure-based alignment of TRP channels

Sequence-based alignment of TRP channels is complicated by low sequence identity, with a previous multiple sequence alignment of TRP channel TM sequences revealing just 16% identity as the major mode of the full multiple sequence alignment (Palovcak et al., 2015). Structure-based alignments are thought to be more reliable than sequence-based alignments, particularly when sequence identity is low (Carpentier and Chomilier, 2019). In addition, structure-based alignments are sensitive to conformational changes and can reveal how residues may change position during ligand binding, channel opening, or other conformational changes. To interrogate relationships of functionally important regions within the TM domains, therefore, we aimed to generate a structure-based alignment for all available TRP channels. The availability of a large number of TRP channel structures allows for a more comprehensive structure-based alignment than has previously been performed for this or other protein families, and we believe that similar structural alignments would provide useful perspective for other protein families with low sequence homology and many available structures.

A total of 136 TRP channel structures have been reported, of which 117 were determined using cryo-EM and 22 using X-ray diffraction. A subset of these structures, however, are of limited resolution and their inclusion would have complicated the analysis. We therefore selected 120 of those structures that were resolved to effective resolutions of 5 Å or better (Figure 2 – Source Data 1) and focused on the TM region, which appears to have a well-conserved architecture across TRP channels. The TM regions of these channels were aligned using Fr-TM-Align (Pandit and Skolnick, 2008; Zhang and Skolnick, 2005), which aligns structures pairwise by optimizing for the global template-modeling-score (TM-score), a measure of backbone fold similarity that is independent of protein length (see Methods). As a fragment-based alignment method, Fr-TM-Align is effective even in cases with large conformational differences (Stamm and Forrest, 2015). Alignments of the TM regions of the TRP family structures generally have TM-scores of >0.6, indicating that they share similar global folds (Figure 2) (Xu and Zhang, 2010). The aligned TRP channel structures also share a common fold with a voltage-activated potassium channel (2r9r; TM-scores ranging from 0.46 to 0.78, with TM-scores <0.6 obtained only for some TRPM and

TRPC structures), consistent with them sharing six TM helices per subunit, a common tetrameric assembly and a domain-swapped architecture. As a negative control, we compared the TRP channels to two structurally-unrelated channels (trimeric P2X3 and pentameric ELIC) (Mansoor et al., 2016; Pan et al., 2012) and obtained TM-scores ranging from 0.08 to 0.40, consistent with the mean TM-score of 0.3 obtained for the best alignments between randomly selected proteins (Zhang and Skolnick, 2004).

The cytoplasmic domains of TRP channels adopt unique folds between subfamilies and thus have been traditionally used to define subfamilies. Nevertheless, sequence analysis of the TM regions alone is sufficient to define TRP channel subfamilies (Palovcak et al., 2015; Yu and Catterall, 2004). To evaluate the quality of our structural alignments we examined whether segregation into subfamilies could be observed using hierarchical clustering based on TM-score alone (Figure 2). With a few notable exceptions, clustering based on TM-score corresponded nicely to existing subfamily assignments, despite the variety of methods of structure determination (X-ray vs cryo-EM) and imaging environments (detergent, amphipol, or nanodisc) used, suggesting that the conditions of structure determination have not introduced substantial artifacts (Figure 2). Where possible, we have directly compared structures of the same complex determined using cryo-EM and X-ray crystallography and observed high TM-scores and close association in the hierarchical clustering, indicating that structures determined by different methods are indeed similar (e.g. apo rTRPV6, TM-score = 0.96 for 6bob and 5wo7; vanilloid agonist-bound TRPV2 quadruple mutant, TM-score = 0.88 for 6oo7 and 6bwj; apo TRPV2, TM-score = 0.87 for 5an8 and 6bwm). Note that, because the TM-score is normalized by the length of the reference protein, the TM-scores for a given pair of proteins are asymmetric depending on which protein is chosen as the reference. As noted in the Methods, we chose to perform hierarchical clustering along the stationary protein axis, so that the TM-scores compared were for different mobile proteins to the same stationary protein.

On the sequence level, the pore domains in TRP channels are highly conserved across all TRP channel subfamilies, whereas the peripheral S1-S4 domains are more variable between subfamilies (Figure 2 – Figure Supp. 3; sequence identity data from Fr-TM-Align pairwise alignments not shown) (Ng et al., 2019; Palovcak et al., 2015; Vinayagam et al., 2018). Consistent

with this pattern, clustering of TRP channel structures into subfamilies was more robust when considering the TM-scores of the peripheral S1-S4 domains compared to those of the pore domain (Figure 2 – Figure Supp. 1 and 2).

In the hierarchical clustering of the entire TM region, the structures determined for *Xenopus laevis* TRPV4 (6bbj) and the rTRPV6 L495Q mutant (5iwk) are notable exceptions because the TM-scores of their alignments with the other TRPV channels were unusually low (0.41 to 0.77 for TRPV4 and 0.32 to 0.73 for rTRPV6 L495Q) (Figure 2). When the pore domain and S1-S4 domains were considered separately, the rTRPV6 L495Q mutant did cluster with the vanilloid subfamily (Figure 2 – Figure Supp. 1 and 2), consistent with the individual domains adopting similar folds and with the global fold dissimilarity in the whole TM region stemming from the rTRPV6 L495Q mutant adopting a non-domain-swapped architecture unlike the wild-type protein (Saotome et al., 2016; Singh et al., 2017). In the case of TRPV4 (Deng et al., 2018), the S1-S4 and pore domains did not cluster with other TRPV channels even when those domains were considered independently (Figure 2 – Figure Supp. 1 and 2), but the reason for this structural distinction is not clear. It will therefore be important to determine additional structures of the TRPV4 channel to determine whether the distinct architecture in the TM region is defining for this subtype. The P2X3 and ELIC channels that served as negative controls were not closely associated with any TRP channels after hierarchical clustering (Figure 2). From this analysis we conclude that our structural alignment of TRP channels is robust and consequently that the backbone folds within the TM regions of these channels are most similar within subfamilies.

To enable comparison of structurally-equivalent residues between TRP channel structures, we used the pairwise alignments of all 119 structures relative to the reference structure of TRPM2 (6co7) to construct a multiple sequence alignment (see Methods; Figure 2 – Figure Supp. 3). TRPM2 was selected as the reference as it contains the longest sequence in the TM regions, which served to maximize the length of the alignment. When compared to a sequence-based alignment of the same TM domain sequences generated using Clustal Omega (Madeira et al., 2019) (see Methods; Figure 2 – Figure Supp. 4), the structure-based alignment identified relationships more accurately between proteins within all six TM helices, even in regions where sequence similarity is low, consistent with previous findings (Carpentier and

Chomilier, 2019). Therefore, the structure-based alignment has been used in subsequent analysis. Relationships are more ambiguous in the reentrant pore loop that forms the ion selectivity filter near the extracellular end of the pore, reflecting considerable structural differences between subfamilies. In addition, the pre-S1 helix found in TRPM channels is unique to that subfamily and thus was not aligned to other TRP channels in this region.

Dimensions of the intracellular S6 gate region in TRP channels

Regulation of ion flow across the membrane is a critical function of TRP channels, so investigation of ion permeation pathways in TRP channel structures is of obvious interest. The two main regions that determine the conductance of the channels are the selectivity filter and the activation gate. With respect to the latter, functional studies examining the accessibility of introduced cysteine residues to thiol-reactive compounds and metals (Salazar et al., 2009), as well as studies examining the state-dependence of blocking ions (Jara-Oseguera et al., 2008; Oseguera et al., 2007), have concluded that the TRPV1 channel opens and closes at the intracellular end of the pore in response to vanilloid binding. A similar S6 activation gate region has been identified in studies of structures determined in the absence of activating ligands for all TRP channel subfamilies, with the exception of a few that have high baseline activity, such as TRPV5 and TRPV6 (Chen et al., 2017; Guo et al., 2017; Hirschi et al., 2017; Jin et al., 2017; Liao et al., 2013; Paulsen et al., 2015; Schmiede et al., 2017; Shen et al., 2016; Tang et al., 2018; Winkler et al., 2017). Therefore, the intracellular end of the pore is of key interest when examining the conduction pathway of TRP channels.

To globally assess ion permeation pathways in TRP channels, we calculated the accessibility of those pathways using HOLE (Smart et al., 1996), further restricting our analysis to structures for which side-chains for all pore-lining residues have been assigned (see Methods; Figure 3; Figure 3 – Figure Supp. 2,3). We also identified those residues responsible for determining the dimensions of the ion permeation pathway and mapped minimum radius values onto the structure-based sequence alignment for S6 and for those elements contributing to the ion selectivity filter (See Methods; Figure 4). In all structures, the intracellular S6 constrictions occur at one or more of four positions spanning three helical turns of the S6 helix, suggesting that depending on the S6 helix conformation, a cytosolic gate could be formed at different sites

(Figure 3; Figure 3 – Figure Supp. 2,3; Figure 4). The deepest of these constrictions within the pore we designated as site A and the one closest to the cytoplasmic surface as site D, with sites B and C being the most common locations of the narrowest S6 constriction across TRP channel subfamilies (Figure 4).

When considering the ability of ions to permeate, we took into account the structural characteristics of the pores, in particular the hydrophobicity and the afforded diameter of the conduction pathway. At a constriction where polar side chains or backbone carbonyls can contribute to ion coordination, such as the extracellular selectivity filter of TRP channels, ions may pass through in a partially or fully dehydrated state, with a lower-bound atomic radius of approximately 1 Å for fully dehydrated Na⁺ or Ca²⁺ ions. At a hydrophobic constriction such as the one formed by the intracellular S6 helix, hydrophobic side chains will not attract ions or facilitate ion dehydration, meaning that ions likely pass the S6 gate in a fully hydrated state with effective radii of > 3 Å for hydrated Na⁺, K⁺, Ca²⁺, and Mg²⁺ ions (Nightingale, 1959).

For all TRP channel structures, the open probability of the construct used for structure determination has not been measured in either the absence or presence of activating stimuli, hindering objective attempts to relate specific structures to distinct functional states. If we consider only the 55 TRP channel structures with no ligands modelled in the structure as representing an apo state (see Methods, Table), 38 contain multiple regions along the intracellular side of the S6 helix at which the pore radius is ≤1.0 Å, too narrow to support permeation of hydrated cations, even considering the inherent dynamics of the structure (Figure 3; Figure 3 -Figure Supp. 2,3; Figure 4). Dehydrated cations are also unlikely to permeate given the hydrophobic nature of the contributing side chains at the S6 constriction. Notably, there are several examples of apo state channel structures in which the pore radius near the intracellular end of the S6 helices is wider than 1.0 Å in structures determined in the absence of an activating stimulus (Figure 3; Figure 3 -Figure Supp. 2,3; Figure 4). Specifically, in the case of TRPV3 and TRPV5, the pore radius within the S6 gate can be as large as 2 Å, whereas for TRPV2, TRPV6, TRPM2, TRPP1 (PKD2) and TRPP2 (PKD2L1) the minimal pore radius can be as large as 3 Å (Figure 3 – Figure Supp. 3). Although some of these S6 gate regions are nearly large enough to allow permeation of hydrated monovalent and divalent permeant cations (radii from 3.3 Å for Na⁺ to

4.1 Å for Ca²⁺), for each of these subtypes other apo structures have been determined with internal pores narrower than a radius of 1.2 Å (Figure 3; Figure 3 -Figure Supp. 2,3; Figure 4). Given that the internal pores in all TRP channels are lined by hydrophobic residues (Figure 4; Figure 4 – Figure Supp. 1), and thus would not attract ions nor facilitate ion dehydration, it seems likely that most of the TRP channel structures discussed thus far represent non-conducting states where the S6 gate is closed. TRPV6 is interesting because this channel has a relatively high open probability in cellular membranes (0.25-0.9 depending on voltage and the concentration of phosphatidylinositol 4,5-bisphosphate, abbreviated PIP₂) (Zakharian et al., 2011), and therefore one would expect the structures would be more likely to correspond to open conformations than for other TRP channels. In fact, many of the TRPV6 structures contain S6 gates narrower than 1.2 Å and thus likely represent closed conformations. However, in all of these cases, the protein used for structure determination contained truncations or mutations that might have influenced the closed-open equilibrium. In contrast, two structures of wild-type TRPV6 and one of the Y467A mutant contain S6 gates with minimal radii of 2.7-3.1 Å, suggesting that they may represent an open, ion-conducting state (McGoldrick et al., 2018). Nevertheless, it is unclear whether opening of the S6 gate to this extent can support a single channel conductance of 30-50 pS, as measured for TRPV6 (Zakharian et al., 2011).

When considering those structures determined in the presence of activators, it is notable that 16 out of 35 contain pores narrower than 1.0 Å radius in the cytoplasmic region, suggesting that they represent non-conducting (possibly desensitized) states (Figure 3; Figure 3 – Figure Supp. 1-4; Figure 4). Only 19 of these activator-bound structures have more dilated internal pores, with radii ranging from 1.2 to 4.4 Å. Of all the TRP channel structures reported thus far, that of TRPM2 bound to its two activators (ADP-ribose and Ca²⁺) is the most likely to represent an open state, as the dimensions of the S6 gate region of TRPM2 (4.4 Å radius) (Zhang et al., 2018a) are similar to those of Kv channel structures widely considered to be open (4.2-15 Å radius) (Hite and MacKinnon, 2017; Long et al., 2007; Tao et al., 2017; Tao and MacKinnon, 2019b; Wang and MacKinnon, 2017) (Figure 3; Figure 3 – Figure Supp. 2). The state of the remaining activator-bound structures is more ambiguous, as dimensions of the S6 gate region range from radii of 3 Å for TRPV1 and TRPV3 to 3.3 Å for TRPV5. In the case of TRPV1, not only is

the single channel conductance quite high (90-100 pS at positive voltages) (Hui et al., 2003; Oseguera et al., 2007; Premkumar et al., 2002), but also quaternary ammonium blocking ions as large as tetrapentyl ammonium (10 Å diameter) must be able to pass the S6 gate when open (Jara-Oseguera et al., 2008; Oseguera et al., 2007), suggesting that the cytoplasmic pore is likely to be larger than a minimal radius of 3 Å. In addition, although the open probability of the construct of TRPV1 used for structure determination is not known, it contains a deletion of the pore-turret that is known to decrease open probability below 0.5 (Geron et al., 2018; Jara-Oseguera et al., 2016).

Surprisingly, there was no striking correlation between the dimensions of the internal pore and whether the protein structure was determined in the absence or presence of activators or inhibitors (Figure 3 – Figure Supp. 1). The prevalence of a cytoplasmic constriction across TRP channel subfamilies supports the prevailing idea that the internal region of S6 functions as a universal gate, and it seems likely that in most instances the structure of a fully open state remains to be determined.

The ion selectivity filter in TRP channels

The extracellular end of the ion permeation pathway is relatively narrow in most structures and across TRP channel subfamilies (Figure 3; Figure 3 – Figure Supp. 2,3), consistent with this region serving as an ion selectivity filter as it does in related tetrameric cation channels (Owsianik et al., 2006). Notably, in several instances such as apo TRPM8, the structure of the selectivity filter is poorly resolved, resulting in large pore radii in our analysis (Yin et al., 2019a; Yin et al., 2018). However, the external end of the pore is better resolved in a recent structure of TRPM8 in the presence of activators (6o77) (Diver et al., 2019), suggesting that this region forms an ion selectivity filter similar to that in other TRP channels, albeit with dimensions that are less narrow (Figure 3 – Figure Supp. 2).

The ion selectivity of TRP channels fits into three broad categories; Ca²⁺ selective (TRPV5 and TRPV6), monovalent cation selective (TRPM4 and TRPM5), and non-selective among cations (all other TRP channels) (Owsianik et al., 2006). To assess whether there is any clear structural correlate to these differences in ion selectivity, we examined the available structures and identified three structural features of the ion selectivity filter that are consistently discernible for

those channels that are non-selective between monovalent and divalent cations, some of which were noted in the original report of the structure of TRPP1 based on a comparison to structures of TRPV1, TRPV2 and TRPA1 (Shen et al., 2016) (Figure 5; Figure 4 – Figure Supp. 1). First, a highly-conserved Gly residue (G643 in TRPV1) is present in non-selective channels after the C-terminal end of the reentrant pore helix and enables a sharp bend in the backbone of the protein (Figure 5; Figure 4 – Figure Supp. 1). Second, two backbone carbonyls are positioned towards the base of the filter where they could interact with permeant ions (Figure 5; Figure 4 – Figure Supp. 1). The presence of backbone carbonyls within a narrow region of the filter is reminiscent of K⁺ channels where ion dehydration is critical for ion permeation and selectivity (Doyle et al., 1998; Zhou et al., 2001). Third, the side chain of an acidic residue or a Gln is positioned immediately adjacent to the extracellular side of the narrowest region of the filter (Figure 5; Figure 4 – Figure Supp. 1). TRPV1-4 channels also contain a second conserved Gly residue within the narrowest region of the filter, which positions the conserved Asp or Gln within the permeation pathway (Figure 4 – Figure Supp. 1). Mutagenesis of the conserved Asp in TRPV1 and TRPV4 channels reduces divalent ion permeability and channel affinity for the inhibitor ruthenium red (Garcia-Martinez et al., 2000; Voets et al., 2002). Although these features are consistently seen in all structures of non-selective TRP channels, the dimensions of the filter vary considerably (with minimal radii from 0.5 to 3.7 Å for structures in which the selectivity filter is resolved) (Figure 3 – Figure Supp. 2,3; Figure 4), raising the possibility that the filters of these TRP channels have intrinsic flexibility. These conserved features of the selectivity filter arise despite low sequence identity or similarity between nonselective TRP channels from different subfamilies (Figure 5 – Figure Supp. 1,2).

Notably, all three of these structural features seen in non-selective TRP channels are discernably different in the two Ca²⁺-selective channels, TRPV5 and TRPV6, as originally noted for the X-ray structure of TRPV6 (Saotome et al., 2016). In place of the conserved Gly after the reentrant pore helix, TRPV5 and TRPV6 contain a conserved Thr residue that contributes its hydroxyl group to the ion permeation pathway (Figure 5; Figure 4 – Figure Supp. 1). In addition, these Ca²⁺-selective channels have a more extended selectivity filter that contains at least three backbone carbonyl groups positioned to line the permeation pathway (Figure 5; Figure 4 – Figure

Supp. 1). The conserved Asp or Gln residues found in the non-selective cation permeable TRP channels is always an Asp in TRPV5 and TRPV6, and mutagenesis of this Asp is known to diminish Ca^{2+} permeation and Mg^{2+} block in TRPV5 (Nilius et al., 2001). Finally, the pore radius is consistently narrower at this region of the filter for those two Ca^{2+} selective channels (Figure 4; Figure 5; Figure 4 – Figure Supp. 1); indeed, density attributable to a divalent ion was identified in this external narrow region in the X-ray structure of TRPV6 (Saotome et al., 2016).

The structure of the monovalent cation-selective TRPM4 channel is intriguing because it exhibits most of the key features seen in the structures of non-selective TRP channels, including the conserved first Gly and two backbone carbonyls within the permeation pathway, and the conserved acidic/Gln position at the external end of the filter is always a Gln (Figure 5; Figure 4 – Figure Supp. 1). The side chain of this Gln was noted to hydrogen bond with the backbone carbonyl of the conserved first Gly in adjacent subunits in one TRPM4 structure, and this network was proposed to stabilize the filter with a diameter large enough to support permeation of hydrated monovalent ions, but not large enough for hydrated divalent ions nor narrow enough to permit ion coordination and dehydration (Guo et al., 2017). Mutation of the conserved Gln to Glu, Asp or Asn disrupts the monovalent cation selectivity of the TRPM4 channel (Guo et al., 2017; Nilius et al., 2005), indicating a critical role of this residue and supporting the proposed mechanism of monovalent cation selectivity. However, it is noteworthy that the dimensions of the filter vary from 1.4 to 2.3 Å in the available TRPM4 structures (Figure 4; Figure 3 – Figure Supp. 2) and no structures have yet been reported for TRPM5 channels, the only other TRP channel that exhibits monovalent cation selectivity. It is interesting that a subset of non-selective channels (e.g. TRPM2 and TRPM8) also contain a Gln at this position, indicating that this residue is not sufficient to determine monovalent cation selectivity and that the dimensions of the pore and the water coordination geometry are likely critical to the mechanism of ion selectivity. A particularly important feature to resolve going forward will be to determine whether ions permeate a given selectivity filter in hydrated or partially dehydrated forms. A reasonable working hypothesis emerging from these structures is that monovalent-selective channels may largely conduct hydrated cations, divalent cation-selective channels may largely conduct dehydrated cations, while non-selective channels may permit both hydrated and dehydrated

forms of cations to permeate. However, a thorough mechanistic understanding of ion permeation in TRP channels will require additional experimental and computational studies to determine the energetic contributions from pore flexibility and nearby charges.

In addition to the heterogeneity in dimensions of the selectivity filters noted above, in several TRP channel structures, the ion selectivity filters clearly adopt distinct conformations in apo state structures compared to those that have activators bound. For example, in the case of TRPV1, the filter has a minimum radius of ~ 0.5 Å in the apo structure but expands to a minimum radius of 2.5 Å in the presence of the activating toxins double-knot toxin and resiniferatoxin (DkTx and RTx, respectively; Figure 3), leading to the proposal that the selectivity filter in TRPV1 might also serve as a gate that regulates ion permeation (Cao et al., 2013; Gao et al., 2016b). The idea of two gates has been extended to other TRP channels in which conformational changes in the ion selectivity filter are discernable, including TRPV2 (Huynh et al., 2016; Zubcevic et al., 2016; Zubcevic et al., 2019b; Zubcevic et al., 2018b) and TRPP2 (PKD2L1) (Grieben et al., 2017; Shen et al., 2016; Su et al., 2018b; Wilkes et al., 2017). A correlate of this proposal is that the apo form would not conduct ions; although the selectivity filters in apo structures of TRPV1 and TRPV2 would be too narrow for hydrated ions to permeate, the dimensions would likely be sufficient for partially dehydrated ions to move through the filter. In addition, the possibility that the selectivity filter functions as a gate in TRPV1-3 channels was recently examined, revealing that thiol-reactive Ag⁺ ions permeated the selectivity filters in the absence of activators, suggesting that the filters of these channels do not efficiently prevent ion permeation in the closed state (Jara-Oseguera et al., 2019). Lending support to ion permeation through narrow selectivity filters are K⁺ channels, where ion dehydration is thought to be central to the mechanism of ion selectivity (Doyle et al., 1998; Zhou et al., 2001) and for which the minimal radii within the selectivity filter are < 1.0 Å for structurally-conserved selectivity filters in different channels (Figure 3; Figure 3 – Figure Supp. 2).

Ligand-binding pockets in TRP channels

TRP channels are activated by a diverse array of chemical ligands and stimuli such as temperature (Clapham, 2007), yet the structures of the TM regions to which many of these activators bind are remarkably similar. Although vanilloid sensitivity has been engineered into both TRPV2 and TRPV3 (Zhang et al., 2016; Zhang et al., 2019), suggesting that the gating

mechanisms of these vanilloid-insensitive TRP channels are similar to those of TRPV1, we currently understand very little else about how the gating mechanisms of different TRP channel subfamilies are related. Out of the 120 available TRP channel structures that we analyzed, 30 were determined in complex with activating ligands contacting the TM region, including vanilloids (e.g. RTx; TRPV1 and TRPV2), DkTx (TRPV1), cooling agents (icilin and WS-12; TRPM8), Ca²⁺ ions (TRPM2, TRPM4 and TRPM8), cannabidiol (CBD; TRPV2), ML-SA1 (TRPML1), 2-aminoethoxydiphenyl borate (2-APB; TRPV3 and TRPV6) and PIP₂ (TRPM8). These structures provide an unprecedented opportunity to explore the structure and conservation of ligand binding sites across different TRP channels. Densities for interacting lipids can also be seen in maps for many TRP channel structures, but we omitted these from our analysis because in most cases the quality of the cryo-EM density is insufficient to unambiguously identify the lipid. To explore the extent to which ligand binding sites are conserved between different TRP channels, for each ligand, we selected a template structure in complex with that ligand, identified any residues with side chain atoms within 4 Å of the ligand and then used our structure-based sequence alignments to examine the corresponding residues in all other structures. For each ligand we defined a sequence motif representing all residues lining the ligand binding pocket regardless of their location along the primary sequence of the channel, calculated the percentage of identical and similar residues in the corresponding motif in all other structures, and generated corresponding heat maps and structure-based sequence alignments (Figure 6; Figure 6 – Figure Supp. 1,2; see Methods).

The vanilloid-binding pocket observed in the TRPV1-RTx complex in nanodiscs (Gao et al., 2016b), and in an engineered TRPV2 channel in detergent (Zubcevic et al., 2018b), is positioned at the interface between the S1-S4 domain of each subunit and the pore-forming S5-S6 domain of the adjacent subunit, with residues in S3, S4, S4-S5 linker, S5 and S6 contacting RTx (Figure 7A,B). RTx is a relatively large ligand, with a surface area of 1,605 Å² and contacts the side chains of 15 aliphatic and aromatic hydrophobic residues and four polar or charged residues in the complex with TRPV1 (Figure 7B). Notably, lipid-facing cavities lined by hydrophobic residues resembling this vanilloid-binding pocket in TRPV1 and TRPV2 can be seen in all TRP channel subfamilies (Figure 6; Figure 6 – Figure Supp. 1). The similar side-chain character of residues lining

the vanilloid-binding pocket in other TRP channels suggests that other hydrophobic ligands might bind to this pocket and raises the possibility that engineering vanilloid sensitivity into other TRP channel subfamilies, as has already been done for TRPV2 and TRPV3 (Zhang et al., 2016; Zhang et al., 2019), might be an informative approach to explore the extent to which gating mechanisms have been conserved. Indeed, the vanilloids capsaicin and capsazepine have been reported to inhibit TRPM8 channels (Behrendt et al., 2004; Weil et al., 2005), possibly by binding to the equivalent pocket, though their site and mechanism of action in the TRPM8 channel have yet to be explored.

DkTx contains two domains, K1 and K2, which bind to the outer perimeter of the pore domain of TRPV1, interacting with residues in the extracellular end of S6 and the reentrant pore helix, as well as with lipids in the surrounding membrane (Figure 7) (Bae et al., 2016; Gao et al., 2016b). Interactions of the toxin with the channel involve a larger surface area than for the other ligands that activate TRP channels, as DkTx has a total surface area of 6377 \AA^2 , with protein-protein interfaces of 655 \AA^2 and 556 \AA^2 for the K1 and K2 domains, respectively (Bae et al., 2016), and involve both hydrophobic and polar interactions. MD simulations of the toxin-channel complex suggest that Y631, F649, T650, N652, D654, F655, K656, A657 and V658 on rTRPV1 interact with DkTx (Bae et al., 2016). Of these, mutations at Y631, F649, T650 and A657 are known to alter activation of the channel by the toxin (Bohlen et al., 2010). Our analysis of a more recent structure in nanodiscs further identifies K535, S629, S632, L635, I660, and I661 as being within 4 \AA of DkTx (Gao et al., 2016b). DkTx is thought to be selective for TRPV1 as the toxin does not activate TRPV2, TRPV3, TRPV4, TRPA1 or TRPM8 (Bohlen et al., 2010). Although the residues in TRPV1 that likely interact with DkTx are not well conserved among other TRP channels (Figure 6; Figure 6 – Figure Supp. 1), the interaction of DkTx with the surrounding lipid membrane is thought to be energetically important for binding (Bae et al., 2016; Sarkar et al., 2018) and could conceivably facilitate binding of the toxin to other TRP channels. Thus, attempting to engineer DkTx-sensitivity into other TRP channels might be a useful approach for exploring the extent to which gating mechanisms are conserved, in particular for channels where conformational changes in the external pore play important roles in gating.

Cryo-EM structures of TRPM8, in complex either with WS-12, a potent analog of menthol, or with both the cooling agent icilin and Ca^{2+} ions, reveal that the cooling agent binding pocket is located close to the vanilloid-binding pocket seen in TRPV1 and TRPV2 (Yin et al., 2019a; Yin et al., 2018). In contrast to the vanilloid site, however, the cooling agent binding pocket is located entirely within the S1-S4 domain, with residues in all four helices and the TRP box contributing to the site (Figure 8). This cooling agent site is exposed to the surrounding membrane between the S2 and S3 helices (partially occluded by an α helix C-terminal to the TRP box), but also to the intracellular aqueous environment, which presumably allows Ca^{2+} ions to access the site from the cytoplasm. The cooling agent binding pocket is considerably smaller than the vanilloid binding pocket (the surface areas of icilin and WS-12 are 788 \AA^2 and 742 \AA^2 , respectively) and contains many polar residues, with two Arg, two Tyr and one His residue positioned with atoms within 4 \AA of the ligands (Figure 8). In addition, in the Ca^{2+} -icilin complex the intracellular end of the S4 helix adopts an alternate conformation that repositions residues in the binding pocket, a difference that is not seen for WS-12 (Yin et al., 2019a), suggesting that different cooling agents have distinct mechanisms of activation. Beyond TRPM8, our analysis shows that residues lining the cooling agent binding pocket in TRPM8 are highly conserved in TRPM2 and TRPM4 structures and somewhat conserved in TRPM7 channels, but are very different in TRPV, TRPML and TRPP channels (Figure 6; Figure 6 – Figure Supp. 1). Although it is unclear whether it would be possible to engineer cooling agent binding sites into other TRP channels given the relatively small size of the cavity and involvement of polar residues, it would be interesting to investigate why TRPM2 and TRPM4 have not been reported to be sensitive to cooling agents.

Intracellular Ca^{2+} regulates the activity of TRPM2, TRPM4 and TRPM8 channels and densities attributed to Ca^{2+} ion have been identified within the S1-S4 domains of all three TRPM channels (Autzen et al., 2018; Diver et al., 2019; Winkler et al., 2017; Yin et al., 2019a; Yin et al., 2018; Zhang et al., 2018a). The Ca^{2+} binding sites identified in these TRPM channels involve Glu, Asp, Gln and Asn residues in S2, S3 and the S4-5 linker, and, in the context of TRPM8, the Ca^{2+} binding site is contiguous with the cooling agent binding pocket, though none of the Ca^{2+} -binding residues directly contact the cooling agents WS-12 or icilin (Figure 8D). Our analysis shows that the Ca^{2+} -coordinating residues are not conserved in TRPV, TRPML or TRPP channels, nor in the

more closely-related TRPM7 channel, similar to the trend observed for the cooling agent binding pocket (Figure 6; Figure 6 – Figure Supp. 1). Interestingly, the Ca²⁺ binding motif is somewhat conserved in TRPC channels (Figure 6; Figure 6 – Figure Supp. 1). Moreover, in cryo-EM structures of TRPC4 and TRPC5 (5z96 and 6aei) densities were identified in the same site, though these densities were tentatively attributed to Na⁺ ions based on buffer composition (Duan et al., 2019; Duan et al., 2018a). TRPC channels have been implicated in intracellular Ca²⁺ signaling (Curcic et al., 2019), but whether Ca²⁺ ions bind directly to the channel and regulate activity remains unclear. It would be interesting to mutate the putative ion binding site in TRPC channels to explore whether Ca²⁺ can directly modulate channel activity through this ion binding site.

The 2-APB binding sites identified in cryo-EM structures of TRPV3 and TRPV6 channels are noteworthy because this ligand functions as either an activator or inhibitor for many different TRP channels and was observed at three distinct sites, designated sites 1-3 (Figure 9) (Singh et al., 2018a; Singh et al., 2018c; Zubcevic et al., 2019a). Site 1 in TRPV3 is located within the cytoplasm at the interface between the TRP helix and the pre-S1 helix (Figure 9C) and mutations in this site also alter the apparent affinity for 2-APB (Singh et al., 2018a; Zubcevic et al., 2019a). Site 2 in TRPV3 is located near the intracellular end of the TM domains between the S1-S4 domain and the TRP helix (Figure 9D), in the vicinity of the cooling agent binding sites in TRPM8 (Singh et al., 2018a). This site is similar to that identified for TRPV6 using X-ray crystallography, and the ligand density was confirmed using a brominated derivative of 2-APB (Singh et al., 2018c). Mutation of a conserved Tyr to Ala in site 2 increases the apparent affinity of 2-APB to TRPV1-3 and to TRPV6, even though the ligand is an activator in TRPV1-3 and an inhibitor in TRPV6 (Singh et al., 2018c). Site 3 in TRPV3 is located towards the extracellular side of the protein between S1 and S3 helices (Singh et al., 2018a)(Figure 9B) but has yet to be studied with mutagenesis. Using our structural alignments, we examined the conservation of all three sites, and found that all three are poorly conserved in other TRP channels (including TRPV6) when compared to TRPV3, and that the 2-APB site in TRPV6 only shows conservation with TRPV5 (Figure 6; Figure 6 – Figure Supp. 2). This lack of conservation is surprising given that 2-APB can modulate the activity of many different TRP channels (as an agonist for TRPV1-3 and TRPM6; as an inhibitor of TRPM2, TRPM3, TRPM8, TRPC5, TRPC6 and TRPV6; as an inhibitor at low concentration and as agonist at

high concentration for TRPM7) (Chokshi et al., 2012; Colton and Zhu, 2007; Hu et al., 2004; Kovacs et al., 2012; Togashi et al., 2008; Xu et al., 2005). Indeed, although specific side chains are poorly conserved, all three 2-APB sites contain multiple Arg, His and hydrophobic residues (Figure 9), suggesting that the structural basis for 2-APB binding (and activity) may rely more on side chain character than on binding pocket shape. Notably, 2-APB has been reported to undergo chemical changes in solution and adopt different pH-dependent configurations, such that different forms might bind to distinct sites or modulate channels differently (Gao et al., 2016a). It would be interesting to further explore potential 2-APB binding sites in other TRP channels with both structural and mutagenesis approaches to better understand the promiscuous and pleiotropic behavior of this ligand.

The final ligand binding site that we considered in the TM domain is located adjacent to the vanilloid binding pocket, at the interface between the S6 helix from one subunit and the neighboring pore loop, S5, and S6 helices. This pocket is lined by hydrophobic residues, including bulky side chains like Phe and Tyr. The phyto-cannabinoid cannabidiol (CBD) was identified in this pocket in structures of TRPV2 (Pumroy et al., 2019), and the agonist ML-SA1 was found in the corresponding location in TRPML1 (Fine et al., 2018; Schmiede et al., 2017) (Figure 9 – Figure Supp. 1). For both channels, the activity of the ligand is modified by mutations in the identified binding pocket (Fine et al., 2018; Pumroy et al., 2019; Schmiede et al., 2017). The hydrophobic character of this pocket is relatively well conserved across TRP channels, with the pocket in the TRPML1 channels containing more polar residues, a feature that is conserved in other TRPML subfamily members that are also sensitive to ML-SA1 (Figure 6; Figure 6 – Figure Supp. 2). Although the activity of CBD has not been widely explored across TRP channels, the ligand modulates the activity of many different ion channel proteins (Ghovanloo et al., 2018; Hassan et al., 2014; Mahgoub et al., 2013; Qin et al., 2008; Ross et al., 2008; Thompson and Kearney, 2016), consistent with binding to a hydrophobic cavity that opens to the lipid bilayer.

Unique secondary structural elements within TM helices in TRP channels

The S1-S6 TM segments in all TRP channels adopt α -helical secondary structure (3.6 residues per turn) over most of their length. Alternative helical conformations in proteins include the 3_{10} helix that comprises three residues per turn and is thus more tightly wound (Riek et al.,

2001), and the π helix that contains 4.6 residues per turn, creating a less-tightly wound bulge (Riek and Graham, 2011; Riek et al., 2001). Although the role of alternate helical conformations is not well understood, the presence of 3_{10} helices within the S4 helices of voltage-activated ion channels is thought to play an important role in the process of voltage sensing because 3_{10} helices position basic residues in different environments compared to an α helix (Long et al., 2007). In TRP channels, bulging helical sections resembling π helices have been commonly observed at the intracellular end of S6 helices and proposed to serve as hinges that facilitate opening of the S6 gate (Kasimova et al., 2018; Palovcak et al., 2015; Zubcevic et al., 2016; Zubcevic and Lee, 2019). Using our structural alignment and the dssp algorithm (Kabsch and Sander, 1983; Touw et al., 2015), we assigned secondary structure to each residue in helices S1-S6 for all TRP channels in our alignment (Figure 10). A high frequency of π -helix-like elements within a relatively narrow region of S6 is readily apparent, consistent with conclusions from a recent review on the role of this alternative helix conformation in gating of TRP channels (Zubcevic and Lee, 2019). However, it was not clear whether the presence of these π -helical residues in the S6 helix correlated with changes in pore size, as might be expected for such a gating mechanism. Taking all structures together, there is a slight positive correlation between pore radius and the length of the S6 π helices (Figure 10 – Figure Supp. 1). Analysis of correlations between pore radius and length of S6 π helices must be interpreted cautiously due to the lack of datapoints with large S6 pore radii or short π helices. From the present analysis, we can say that structures with small pore radii can be observed to have either fully α -helical or partially π -helical character in the S6 region. Further structural studies in search of states with wider pores will be needed to clarify the role of π helices in gating. We also note that 3_{10} helices are commonly found at the intracellular end of the S4 helices across all TRP channel subfamilies (Figure 10), similar to what has been observed with the corresponding TM helices in voltage-activated ion channels. Notably, these 3_{10} helices within S4 are observed regardless of whether structures were determined in the presence or absence of activators (Figure 10). Finally, our analysis detects π helices within the S5 helices of TRP channels spatially close to where they are observed in S6 helices, in particular in the TRPV subfamily of TRP channels. The presence of alternative helical conformations within TM regions of TRP channel structures is interesting and should motivate further exploration of their functional roles.

Discussion

The goal of the present study was to construct a structure-based alignment of the TM domains of available TRP channel structures using a uniform approach that allows systematic comparison of structural features in functionally important regions. Our analysis strongly supports the prevailing view that the intracellular end of the S6 helices forms a constriction or gate that prevents ion permeation in closed or non-conducting desensitized states, with the narrowest constrictions occurring at one of four positions along the S6 helices. It remains to be determined if the formation of some of these constrictions is specific to certain TRP channel subtypes. In addition, global analysis of the dimensions of the S6 gate region lead us to suggest that the open states for most TRP channels remain to be elucidated. The internal pore of TRPM2 when bound by Ca^{2+} and ADP ribose has a radius of 4.4 Å and thus is likely large enough to permit rapid diffusion of hydrated cations, consistent with the structure representing an open state. The internal S6 region for TRPV1, TRPV3 and TRPV5 are between 3 and 3.3 Å, which does not seem quite open enough to support permeation of hydrated cations (with large single channel conductance) or the entry of large quaternary ammonium ion blockers. A similar conundrum has been raised by the structures of many K^+ channels. That is, although the S6 gate regions of some K^+ channels have large radii consistent with an open state (e.g. 4.2 Å for Kv1.2/2.1 paddle chimera, 5 Å for hERG, 10 Å for Slo2 and 15 Å for hSlo1 with Ca^{2+}) (Hite and MacKinnon, 2017; Long et al., 2007; Tao et al., 2017; Tao and MacKinnon, 2019b; Wang and MacKinnon, 2017), in other cases the internal pores are narrower than expected (2.5 Å for Kir2.2, 3.5 Å for SK, 3-3.5 Å for GIRK2, 3 Å for KvAP and 2.5 Å for KCNQ1) (Hansen et al., 2011; Lee and MacKinnon, 2018; Sun and MacKinnon, 2020; Tao and MacKinnon, 2019a; Whorton and MacKinnon, 2013) under conditions expected to favor open states (Figure 3 – Figure Supp. 2). It will be important to see whether structures of most TRP channels and some K^+ channels can be determined with more open S6 gates. Solving structures of open states of TRP channels is particularly critical for understanding the structural basis by which different stimuli lead to channel opening, and we propose that future structural studies should focus on increasing construct open probability to facilitate a larger number of open-state particles on cryo-EM grids.

Another fascinating question concerns the mechanisms by which the external selectivity filters in TRP channels can select for monovalent cations (TRPM4 and TRPM5), divalent cations (TRPV5 and TRPV6) or support the permeation of both (all other TRP channels). The X-ray structure of TRPV6 (divalent selective) (Saotome et al., 2016) and a cryo-EM structure of TRPM4 (monovalent selective) (Guo et al., 2017) have led to interesting working hypotheses for these two classes of ion selectivity. In the case of TRPV6, divalent ions can be seen to bind within a narrow region of the filter that would require at least partial dehydration of the ion, suggesting that ion coordination and dehydration are critical to the mechanism of divalent ion selectivity. In the case of TRPM4, evidence of intersubunit hydrogen bonds within the filter lead to the proposal that the filter in monovalent selective TRP channels is structurally rigid and just large enough for hydrated monovalent ions to permeate. Although the filters of non-selective TRP channel have conserved features as noted earlier, the dimensions of the filters are remarkably varied when comparing structures within or between subfamilies and their lack of selectivity might suggest that both hydrated and dehydrated ions may permeate. Clearly higher resolution X-ray structures, where ion binding sites can be examined, will be needed to deduce the underlying mechanisms, and it will be critical to obtain evidence for whether ion permeation involves hydrated or dehydrated forms of permeant cations. Higher resolution structures will also facilitate molecular dynamics simulations to probe the energetics of ion permeation, including contributions from conformational flexibility and electrostatics of nearby charges.

The wealth of available TRP channel structures underscores the extent to which the S1-S4 domain, as well as the interface of this domain with the S5-S6 pore-forming domain and the TRP box functions as a hot spot for ligands to promote opening of TRP channels. This region includes the vanilloid binding pocket in TRPV1, which is also hydrophobic in other TRP channels, perhaps reflecting a common lipid binding site that regulates the activity of many TRP channels. The Ca^{2+} and cooling agent binding sites in TRPM channels are also in close proximity and are relatively well conserved in the TRPM subfamily. Finally, sites 1 and 2 for the promiscuous regulator 2-APB are also positioned nearby, either below or above the TRP helix, respectively. Although the conservation of ligand binding sites varies considerably across different TRP

channels, it would be fascinating to attempt to engineer in ligand sensitivity into insensitive TRP channels to explore the extent to which gating mechanisms are related.

The binding of lipids to TRP channels and regulation of functional activity is a fascinating and emerging area in the field. Although we have not focused on lipid binding sites because the quality of lipid-like densities is not high enough to identify the molecule definitively in most structures, there are a few notable exceptions. In cryo-EM structures of TRPV1 in nanodiscs, several well-defined phospholipid densities can be seen to interact simultaneously with the external membrane-exposed surface of the protein and the tarantula toxin DkTx (Gao et al., 2016b). In an apo structure of TRPV1 in nanodiscs (5irz), as well as structures of TRPC4 (5z96), TRPM2 (6co7), TRPM4 (6bwi, 6bqr, 6bqv), TRPM7 (5zx5, 6bwd), NOMPC (5vkq), TRPP1 (5mke, 5mkf), TRPV5 (6dmr, 6dmu) and TRPV6 (6bo8) lipid density can be seen in the vanilloid binding pocket (Autzen et al., 2018; Duan et al., 2018a; Duan et al., 2018b; Duan et al., 2018c; Gao et al., 2016b; Hughes et al., 2018b; Jin et al., 2017; McGoldrick et al., 2018; Wilkes et al., 2017; Zhang et al., 2018b). Finally, a well-resolved molecule of PIP₂ can also be seen in TRPM8 channels close to where Ca²⁺ and cooling agents bind, and involving basic residues in the pre-S1 helix, the S4-S5 linker, the TRP domain and the cytoplasmic MHR4 domain (Figure 8C). This PIP₂ binding pocket is conserved in TRPM, TRPC, and, to a lesser extent, TRPV channels (Figure 6; Figure 6 – Figure Supp. 1). Lipid-like density was observed at a similar site in TRPM2 (Yin et al., 2019a). PIP₂ is thought to be required for activation of both TRPM2 and TRPM8; indeed, exogenous PIP₂ analogs are sufficient to activate the TRPM8 channel at room temperature (Liu and Qin, 2005; Yudin and Rohacs, 2012).

We undertook a global alignment of TRP channels structures to explore those features that are common to all TRP channels and those that may be unique to specific subfamily members. At the time we stopped adding structures to our alignment, there were 136 structures published over a six-year period. Although this represents an unparalleled number of related ion channel structures to work with, we were surprised that our analysis identifies the need for additional structures, even for the TRPV and TRPM subtypes that dominate our structural alignment. In addition, for most TRP channels it seems that fully open states have yet to be determined. We need additional structures of TRPM4 and TRPM5 to test mechanisms of

monovalent cation selectivity, structures of TRPV5 and TRPV6 to interrogate mechanisms of divalent ion selectivity, and more structures bound to promiscuous modulators such as 2-APB. Those structures that have thus far been determined in lipid nanodiscs have begun to reveal key structural and functional roles of membrane lipids, and this is a particularly important area for further exploration.

Methods

TRP channel structure selection

All TRP channel structures were identified by searching the PDB using the query “TRP channel” on October 31st, 2019 (Berman et al., 2000). Structures with resolution poorer than 5 Å, as well as most non-domain-swapped mutant structures were excluded. Structures available from OPM (Orientation of Proteins in Membranes) were pulled from that database, and those that were not already available were analyzed using the PPM (Positioning of Proteins in Membranes) server (Lomize et al., 2011). The available cryo-EM structures only approach atomic resolution as determined by Fourier shell correlation, and EM electron density maps vary in quality in different regions. However, due to the large number of structures, comparing the structures collectively decreases the impact of random errors in model fitting due to insufficient density map resolvability.

Structure file processing and domain definitions

Only transmembrane domains were used for alignment, so intra- and extra-cellular domains were identified and stripped. For structural alignments, several different regions of the proteins were defined, as follows. TM domains were defined as residues from the start of the pre-S1 domain to the end of the TRP box as determined by visual inspection of the structures (see Figure 2 – Source Data 1 for exact residues used). Pore domain definitions included all residues from the start of the S5 helix to the end of the S6 helix based on the results from OPM or PPM (see above). The S1-S4 domain was defined as all residues from the start of the S1 helix to the end of the S4 helix, based on OPM-identified TM segments. To exclude extramembraneous domains, any loop connecting two OPM-defined TM segments with >100 residues was truncated to leave only the ten residues on each side of the loop nearest to the TM segments. HETATOM entries were also removed. Alignments of the TM domain or pore domain included the entire tetrameric assembly. Prior to alignment, the ordering of the chain identifiers was standardized (counterclockwise as viewed from the extracellular side of the membrane), and chains were then combined into a single chain for compatibility with Fr-TM-Align. Alignments of S1-S4 domains included a single protomer, with all other chains deleted. Non-TRP channels were processed similarly (see Figure 2 – Source Data 1 for exact residues used). Structures were also categorized

qualitatively into groups based on subfamily, experimental method, sample conditions, and ligand-binding state (see Figure 2 – Source Data 1 for category assignments).

Structure-based alignment

To obtain a structure-based, sequence-agnostic sequence alignment, structures were first aligned pairwise using Fr-TM-Align version 1.0, a fragment-based alignment approach that aligns residues based on patterns of secondary structure (Pandit and Skolnick, 2008). Fr-TM-Align has been tested on membrane proteins and is robust even to large conformational changes (Stamm and Forrest, 2015). As with other methods, the aligned structures are iteratively aligned and scored for alignment match before the alignment with the best pairwise TM-score is chosen. The TM-score is a length-independent analogue of RMSD, and indicates global protein fold similarity, with 1.0 indicating identical structures and an average of 0.3 for randomly-selected proteins, where TM-scores above 0.6 indicate a common fold (Xu and Zhang, 2010; Zhang and Skolnick, 2004). Fr-TM Align also reports the transformation matrix for each pairwise structural alignment. TM-scores are normalized to the length of the stationary protein in the pairwise mobile-stationary alignment, resulting in asymmetrical scores depending on which protein of the pair is used as the mobile structure and which as the stationary structure. Therefore Fr-TM-Align was performed twice for each pair of proteins, exchanging the mobile and stationary structures. Mobile and stationary proteins are represented along the vertical and horizontal axes, respectively, in the heatmaps of Figure 2 and Figure 2 – Figure Supp. 1 and 2.

Clustering

Clustering was performed along the stationary axis in the TM-score heatmap. TM-scores were converted into pseudo-distance scores where: $TM\text{-distance} = 1 - TM\text{-score}$, and hierarchical clustering based on TM-distance was calculated with Seaborn's clustermap function using the Nearest Point Algorithm in Euclidean space (parameters: method='single', metric='euclidean', Seaborn version 0.9.0) (Müllner, 2011; Waskom et al., 2018).

Creating structure-based multiple sequence alignments

Residues considered in the TM domain alignment were used to build multiple sequence alignments. One sequence was chosen as the reference (TRPM2, 6co7), while all other proteins were added according to their pairwise alignment with the reference using pyali version 0.1.1

(christang, 2019). Residues that did not align with an amino acid in the reference structure, i.e. insertions, were omitted from the multiple sequence alignment.

Creating sequence-based multiple sequence alignment

The same amino acid sequences used for the structure-based alignment were aligned with ClustalOmega using default settings (Madeira et al., 2019). To enable comparison between structure-based and sequence-based alignments, any residues that did not align with an amino acid in 6co7 were omitted from the sequence-based alignment.

Determining secondary structure and pore radius

Pore dimensions were estimated using HOLE version 2.0, which reports, for each point along the length of the pore, the radius of the largest sphere that can be fit in the pore without intersecting with a neighboring atom, as defined by its van der Waals radius (Smart et al., 1996). Hydrogen atoms were not considered in this analysis. Residues were identified as lining the pore if the distance between any of its atoms and the axis of the HOLE profile was equal to the sum of the van der Waals radius of that atom and the pore radius at that point. The minimum pore radius for a given residue is defined as the smallest radius of the HOLE plot assigned to any atom in that residue.

The DSSP algorithm version 3.0.0 was used to assign the secondary structure of each residue of the protein (Kabsch and Sander, 1983; Touw et al., 2015).

Identifying and analyzing selectivity filters

Selectivity filters were determined by visual inspection and consensus among structures (Figure 4). Selectivity filters were compared pairwise for all structures, with percent identity determined by the number of identical residues, excluding gaps, in equivalent positions. Similarity was defined by a positive score in the BLOSUM62 matrix (Henikoff and Henikoff, 1992).

$$Identity_{\%} = 100\% * \frac{n_{identical}}{n_{ref}}$$

$$Similarity_{\%} = 100\% * \frac{n_{similar}}{n_{ref}}$$

Identifying and analyzing ligand binding pockets

Structures lacking ligands were considered to be in their apo states. For structures that contained ligands, any amino acid with any side-chain atom within 4 Å of the ligand molecule was

considered part of the ligand binding pocket. Equivalent residues in other structures were identified using the structure-based multiple sequence alignment. To calculate percent identity and similarity of the binding pocket residues, one ligand-bound structure was chosen to provide the reference ligand binding pocket motif, and binding pockets from all other structures were analyzed to determine the percentage of residues that were identical or similar to those in the equivalent position in the reference. Identity and similarity were defined as for selectivity filters, above.

Generating figures

All figures of protein structures were created after aligning each structure to the reference structure (TRM2, 6co7) using Fr-TM-Align as described above. For visualization of the entire structure, the corresponding transformation matrix was reapplied in PyMOL version 2.2.3 (Schrödinger, 2015). Analysis and visualization were performed in Python 3.6.7 using Anaconda 5.2.0 packages: SciPy 1.1.0, Matplotlib 2.2.2, pandas 0.24.2, seaborn 0.9.0, Numpy 1.14.3, pyali 0.1.1, HOLE 2.0 implemented with MDAnalysis 0.18.0, DSSP 3.0.0 and Biopython 1.72 (Cock et al., 2009; Hamelryck and Manderick, 2003; Hunter, 2007; McKinney, 2010; Schrödinger, 2015; Virtanen et al., 2020; Waskom et al., 2018). All sequence alignments were visualized with Jalview 2.10.5 (Waterhouse et al., 2009).

Acknowledgments: We thank Joe Mindell, Mark Mayer and members of the Swartz laboratory for helpful discussions.

Funding: This research was supported by the Intramural Research Programs of the NINDS, NIH, Bethesda, MD to LRF and KJS.

Competing interests: Kenton Swartz is a Senior Editor at eLife. Lucy Forrest is a Reviewing Editor at eLife.

Data and materials availability: All data needed to evaluate the conclusions in this paper are available in the main text and supplementary materials.

Author contributions:

Conceptualization (KEH, AA, AO, LRF, KJS), Data curation (KEH), Formal analysis (KEH, AA), Funding acquisition (LRF, KJS), Investigation (KEH, AA, AO, LRF, KJS), Methodology (KEH, AA, LRF, KJS), Project administration (AA, LRF, KJS), Resources (LRF, KJS), Supervision (AA, LRF, KJS), Validation (KEH, AA, AO, LRF, KJS), Writing – original draft (KEH, KJS), Writing – review and editing (KEH, AA, AO, LRF, KJS)

REFERENCES

- Autzen, H.E., Myasnikov, A.G., Campbell, M.G., Asarnow, D., Julius, D., and Cheng, Y. (2018). Structure of the human TRPM4 ion channel in a lipid nanodisc. *Science* 359, 228-232.
- Bae, C., Anselmi, C., Kalia, J., Jara-Oseguera, A., Schwieters, C.D., Krepkiy, D., Won Lee, C., Kim, E.H., Kim, J.I., Faraldo-Gomez, J.D., *et al.* (2016). Structural insights into the mechanism of activation of the TRPV1 channel by a membrane-bound tarantula toxin. *Elife* 5.
- Behrendt, H.J., Germann, T., Gillen, C., Hatt, H., and Jostock, R. (2004). Characterization of the mouse cold-menthol receptor TRPM8 and vanilloid receptor type-1 VR1 using a fluorometric imaging plate reader (FLIPR) assay. *Br J Pharmacol* 141, 737-745.
- Berman, H.M., Westbrook, J., Feng, Z., Gilliland, G., Bhat, T.N., Weissig, H., Shindyalov, I.N., and Bourne, P.E. (2000). The Protein Data Bank. *Nucleic Acids Research* 28, 235-242.
- Bohlen, C.J., Priel, A., Zhou, S., King, D., Siemens, J., and Julius, D. (2010). A bivalent tarantula toxin activates the capsaicin receptor, TRPV1, by targeting the outer pore domain. *Cell* 141, 834-845.
- Cao, E., Liao, M., Cheng, Y., and Julius, D. (2013). TRPV1 structures in distinct conformations reveal activation mechanisms. *Nature* 504, 113-118.
- Carpentier, M., and Chomilier, J. (2019). Protein multiple alignments: sequence-based versus structure-based programs. *Bioinformatics* 35, 3970-3980.
- Chen, Q., She, J., Zeng, W., Guo, J., Xu, H., Bai, X.C., and Jiang, Y. (2017). Structure of mammalian endolysosomal TRPML1 channel in nanodiscs. *Nature* 550, 415-418.
- Chokshi, R., Fruasaha, P., and Kozak, J.A. (2012). 2-aminoethyl diphenyl borinate (2-APB) inhibits TRPM7 channels through an intracellular acidification mechanism. *Channels (Austin)* 6, 362-369.
- christang (2019). pyali (<https://github.com/christang/pyali>).
- Clapham, D.E. (2007). SnapShot: mammalian TRP channels. *Cell* 129, 220.
- Cock, P.J.A., Antao, T., Chang, J.T., Chapman, B.A., Cox, C.J., Dalke, A., Friedberg, I., Hamelryck, T., Kauff, F., Wilczynski, B., *et al.* (2009). Biopython: freely available Python tools for computational molecular biology and bioinformatics. *Bioinformatics* 25, 1422-1423.
- Colton, C.K., and Zhu, M.X. (2007). 2-Aminoethoxydiphenyl Borate as a Common Activator of TRPV1, TRPV2, and TRPV3 Channels. In *Transient Receptor Potential (TRP) Channels*, V.N. Flockerzi, Bernd, ed. (Berlin, Heidelberg: Springer).

Cosens, D.J., and Manning, A. (1969). Abnormal electroretinogram from a *Drosophila* mutant. *Nature* *224*, 285-287.

Curcic, S., Schober, R., Schindl, R., and Groschner, K. (2019). TRPC-mediated Ca²⁺ signaling and control of cellular functions. *Semin Cell Dev Biol* *94*, 28-39.

Dang, S., van Goor, M.K., Asarnow, D., Wang, Y., Julius, D., Cheng, Y., and van der Wijk, J. (2019). Structural insight into TRPV5 channel function and modulation. *Proc Natl Acad Sci U S A* *116*, 8869-8878.

Deng, Z., Paknejad, N., Maksaev, G., Sala-Rabanal, M., Nichols, C.G., Hite, R.K., and Yuan, P. (2018). Cryo-EM and X-ray structures of TRPV4 reveal insight into ion permeation and gating mechanisms. *Nat Struct Mol Biol* *25*, 252-260.

Diver, M.M., Cheng, Y., and Julius, D. (2019). Structural insights into TRPM8 inhibition and desensitization. *Science* *365*, 1434-1440.

Dosey, T.L., Wang, Z., Fan, G., Zhang, Z., Serysheva, I., Chiu, W., and Wensel, T.G. (2019). Structures of TRPV2 in distinct conformations provide insight into role of the pore turret. *Nat Struct Mol Biol* *26*, 40-49.

Doyle, D.A., Morais Cabral, J., Pfuetzner, R.A., Kuo, A., Gulbis, J.M., Cohen, S.L., Chait, B.T., and MacKinnon, R. (1998). The structure of the potassium channel: molecular basis of K⁺ conduction and selectivity. *Science* *280*, 69-77.

Duan, J., Li, J., Chen, G.L., Ge, Y., Liu, J., Xie, K., Peng, X., Zhou, W., Zhong, J., Zhang, Y., *et al.* (2019). Cryo-EM structure of TRPC5 at 2.8-Å resolution reveals unique and conserved structural elements essential for channel function. *Sci Adv* *5*, eaaw7935.

Duan, J., Li, J., Zeng, B., Chen, G.L., Peng, X., Zhang, Y., Wang, J., Clapham, D.E., Li, Z., and Zhang, J. (2018a). Structure of the mouse TRPC4 ion channel. *Nat Commun* *9*, 3102.

Duan, J., Li, Z., Li, J., Hulse, R.E., Santa-Cruz, A., Valinsky, W.C., Abiria, S.A., Krapivinsky, G., Zhang, J., and Clapham, D.E. (2018b). Structure of the mammalian TRPM7, a magnesium channel required during embryonic development. *Proceedings of the National Academy of Sciences* *115*, E8201-E8210.

Duan, J., Li, Z., Li, J., Santa-Cruz, A., Sanchez-Martinez, S., Zhang, J., and Clapham, D.E. (2018c). Structure of full-length human TRPM4. *Proc Natl Acad Sci U S A* *115*, 2377-2382.

Fan, C., Choi, W., Sun, W., Du, J., and Lu, W. (2018). Structure of the human lipid-gated cation channel TRPC3. *Elife* *7*.

Fine, M., Schmiege, P., and Li, X. (2018). Structural basis for PtdInsP₂-mediated human TRPML1 regulation. *Nat Commun* *9*, 4192.

Gao, L., Yang, P., Qin, P., Lu, Y., Li, X., Tian, Q., Li, Y., Xie, C., Tian, J.-b., Zhang, C., *et al.* (2016a). Selective potentiation of 2-APB-induced activation of TRPV1-3 channels by acid. *Scientific reports* 6, 20791-20791.

Gao, Y., Cao, E., Julius, D., and Cheng, Y. (2016b). TRPV1 structures in nanodiscs reveal mechanisms of ligand and lipid action. *Nature* 534, 347.

Garcia-Martinez, C., Morenilla-Palao, C., Planells-Cases, R., Merino, J.M., and Ferrer-Montiel, A. (2000). Identification of an aspartic residue in the P-loop of the vanilloid receptor that modulates pore properties. *J Biol Chem* 275, 32552-32558.

Geron, M., Kumar, R., Zhou, W., Faraldo-Gomez, J.D., Vasquez, V., and Priel, A. (2018). TRPV1 pore turret dictates distinct DkTx and capsaicin gating. *Proc Natl Acad Sci U S A* 115, E11837-E11846.

Ghovanloo, M.R., Shuart, N.G., Mezeyova, J., Dean, R.A., Ruben, P.C., and Goodchild, S.J. (2018). Inhibitory effects of cannabidiol on voltage-dependent sodium currents. *J Biol Chem* 293, 16546-16558.

Grieben, M., Pike, A.C., Shintre, C.A., Venturi, E., El-Ajouz, S., Tessitore, A., Shrestha, L., Mukhopadhyay, S., Mahajan, P., Chalk, R., *et al.* (2017). Structure of the polycystic kidney disease TRP channel Polycystin-2 (PC2). *Nat Struct Mol Biol* 24, 114-122.

Guo, J., She, J., Zeng, W., Chen, Q., Bai, X.C., and Jiang, Y. (2017). Structures of the calcium-activated, non-selective cation channel TRPM4. *Nature* 552, 205-209.

Hamelryck, T., and Manderick, B. (2003). PDB file parser and structure class implemented in Python. *Bioinformatics* 19, 2308-2310.

Hansen, S.B., Tao, X., and MacKinnon, R. (2011). Structural basis of PIP₂ activation of the classical inward rectifier K⁺ channel Kir2.2. *Nature* 477, 495-498.

Hassan, S., Eldeeb, K., Millns, P.J., Bennett, A.J., Alexander, S.P., and Kendall, D.A. (2014). Cannabidiol enhances microglial phagocytosis via transient receptor potential (TRP) channel activation. *Br J Pharmacol* 171, 2426-2439.

Henikoff, S., and Henikoff, J.G. (1992). Amino acid substitution matrices from protein blocks. *Proceedings of the National Academy of Sciences* 89, 10915-10919.

Hirschi, M., Herzik, M.A., Jr., Wie, J., Suo, Y., Borschel, W.F., Ren, D., Lander, G.C., and Lee, S.Y. (2017). Cryo-electron microscopy structure of the lysosomal calcium-permeable channel TRPML3. *Nature* 550, 411-414.

Hite, R.K., and MacKinnon, R. (2017). Structural Titration of Slo2.2, a Na⁽⁺⁾-Dependent K⁽⁺⁾ Channel. *Cell* 168, 390-399 e311.

Hu, H.-Z., Gu, Q., Wang, C., Colton, C.K., Tang, J., Kinoshita-Kawada, M., Lee, L.-Y., Wood, J.D., and Zhu, M.X. (2004). 2-Aminoethoxydiphenyl Borate Is a Common Activator of TRPV1, TRPV2, and TRPV3. *Journal of Biological Chemistry* 279, 35741-35748.

Huang, Y., Winkler, P.A., Sun, W., Lu, W., and Du, J. (2018). Architecture of the TRPM2 channel and its activation mechanism by ADP-ribose and calcium. *Nature* 562, 145-149.

Hughes, T.E., Del Rosario, J.S., Kapoor, A., Yazici, A.T., Yudin, Y., Fluck, E.C., 3rd, Filizola, M., Rohacs, T., and Moiseenkova-Bell, V.Y. (2019). Structure-based characterization of novel TRPV5 inhibitors. *Elife* 8.

Hughes, T.E.T., Lodowski, D.T., Huynh, K.W., Yazici, A., Del Rosario, J., Kapoor, A., Basak, S., Samanta, A., Han, X., Chakrapani, S., *et al.* (2018a). Structural basis of TRPV5 channel inhibition by econazole revealed by cryo-EM. *Nat Struct Mol Biol* 25, 53-60.

Hughes, T.E.T., Pumroy, R.A., Yazici, A.T., Kasimova, M.A., Fluck, E.C., Huynh, K.W., Samanta, A., Molugu, S.K., Zhou, Z.H., Carnevale, V., *et al.* (2018b). Structural insights on TRPV5 gating by endogenous modulators. *Nature Communications* 9, 4198.

Hui, K., Liu, B., and Qin, F. (2003). Capsaicin activation of the pain receptor, VR1: multiple open states from both partial and full binding. *Biophys J* 84, 2957-2968.

Hulse, R.E., Li, Z., Huang, R.K., Zhang, J., and Clapham, D.E. (2018). Cryo-EM structure of the polycystin 2-I1 ion channel. *Elife* 7.

Hunter, J.D. (2007). Matplotlib: A 2D Graphics Environment. *Computing in Science & Engineering* 9, 90-95.

Huynh, K.W., Cohen, M.R., Jiang, J., Samanta, A., Lodowski, D.T., Zhou, Z.H., and Moiseenkova-Bell, V.Y. (2016). Structure of the full-length TRPV2 channel by cryo-EM. *Nat Commun* 7, 11130.

Jara-Oseguera, A., Bae, C., and Swartz, K.J. (2016). An external sodium ion binding site controls allosteric gating in TRPV1 channels. *Elife* 5.

Jara-Oseguera, A., Huffer, K.E., and Swartz, K.J. (2019). The ion selectivity filter is not an activation gate in TRPV1-3 channels. *Elife* 8.

Jara-Oseguera, A., Llorente, I., Rosenbaum, T., and Islas, L.D. (2008). Properties of the inner pore region of TRPV1 channels revealed by block with quaternary ammoniums. *J Gen Physiol* 132, 547-562.

Jin, P., Bulkley, D., Guo, Y., Zhang, W., Guo, Z., Huynh, W., Wu, S., Meltzer, S., Cheng, T., Jan, L.Y., *et al.* (2017). Electron cryo-microscopy structure of the mechanotransduction channel NOMPC. *Nature* 547, 118-122.

- Kabsch, W., and Sander, C. (1983). Dictionary of protein secondary structure: Pattern recognition of hydrogen-bonded and geometrical features. *Biopolymers* 22, 2577-2637.
- Kasimova, M.A., Yazici, A.T., Yudin, Y., Granata, D., Klein, M.L., Rohacs, T., and Carnevale, V. (2018). A hypothetical molecular mechanism for TRPV1 activation that invokes rotation of an S6 asparagine. *Journal of General Physiology* 150, 1554-1566.
- Kovacs, G., Montalbetti, N., Simonin, A., Danko, T., Balazs, B., Zsembery, A., and Hediger, M.A. (2012). Inhibition of the human epithelial calcium channel TRPV6 by 2-aminoethoxydiphenyl borate (2-APB). *Cell Calcium* 52, 468-480.
- Lee, C.H., and MacKinnon, R. (2018). Activation mechanism of a human SK-calmodulin channel complex elucidated by cryo-EM structures. *Science* 360, 508-513.
- Liao, M., Cao, E., Julius, D., and Cheng, Y. (2013). Structure of the TRPV1 ion channel determined by electron cryo-microscopy. *Nature* 504, 107-112.
- Liu, B., and Qin, F. (2005). Functional control of cold- and menthol-sensitive TRPM8 ion channels by phosphatidylinositol 4,5-bisphosphate. *J Neurosci* 25, 1674-1681.
- Lomize, M.A., Pogozheva, I.D., Joo, H., Mosberg, H.I., and Lomize, A.L. (2011). OPM database and PPM web server: resources for positioning of proteins in membranes. *Nucleic Acids Research* 40, D370-D376.
- Long, S.B., Tao, X., Campbell, E.B., and MacKinnon, R. (2007). Atomic structure of a voltage-dependent K⁺ channel in a lipid membrane-like environment. *Nature* 450, 376-382.
- Madeira, F., Park, Y.M., Lee, J., Buso, N., Gur, T., Madhusoodanan, N., Basutkar, P., Tivey, A.R.N., Potter, S.C., Finn, R.D., *et al.* (2019). The EMBL-EBI search and sequence analysis tools APIs in 2019. *Nucleic acids research* 47, W636-W641.
- Mahgoub, M., Keun-Hang, S.Y., Sydorenko, V., Ashoor, A., Kabbani, N., Al Kury, L., Sadek, B., Howarth, C.F., Isaev, D., Galadari, S., *et al.* (2013). Effects of cannabidiol on the function of alpha7-nicotinic acetylcholine receptors. *Eur J Pharmacol* 720, 310-319.
- Mansoor, S.E., Lu, W., Oosterheert, W., Shekhar, M., Tajkhorshid, E., and Gouaux, E. (2016). X-ray structures define human P2X(3) receptor gating cycle and antagonist action. *Nature* 538, 66-71.
- McGoldrick, L.L., Singh, A.K., Demirkhanyan, L., Lin, T.Y., Casner, R.G., Zakharian, E., and Sobolevsky, A.I. (2019). Structure of the thermo-sensitive TRP channel TRP1 from the alga *Chlamydomonas reinhardtii*. *Nat Commun* 10, 4180.
- McGoldrick, L.L., Singh, A.K., Saotome, K., Yelshanskaya, M.V., Twomey, E.C., Grassucci, R.A., and Sobolevsky, A.I. (2018). Opening of the human epithelial calcium channel TRPV6. *Nature* 553, 233-237.

McKinney, W. (2010). Data structures for statistical computing in Python. Paper presented at: SciPy (Austin, TX).

Montell, C. (2011). The history of TRP channels, a commentary and reflection. *Pflugers Arch* 461, 499-506.

Moran, M.M. (2018). TRP Channels as Potential Drug Targets. *Annu Rev Pharmacol Toxicol* 58, 309-330.

Müllner, D. (2011). Modern hierarchical, agglomerative clustering algorithms. In arXiv.

Ng, L.C.T., Vien, T.N., Yarov-Yarovoy, V., and DeCaen, P.G. (2019). Opening TRPP2 (PKD2L1) requires the transfer of gating charges. *Proceedings of the National Academy of Sciences* 116, 15540-15549.

Nightingale, E.R. (1959). Phenomenological Theory of Ion Solvation. Effective Radii of Hydrated Ions. *The Journal of Physical Chemistry* 63, 1381-1387.

Nilius, B., and Flockerzi, V. (2014). Mammalian transient receptor potential (TRP) cation channels. Preface. *Handbook of experimental pharmacology* 223, v - vi.

Nilius, B., Owsianik, G., Voets, T., and Peters, J.A. (2007). Transient receptor potential cation channels in disease. *Physiol Rev* 87, 165-217.

Nilius, B., Prenen, J., Janssens, A., Owsianik, G., Wang, C., Zhu, M.X., and Voets, T. (2005). The selectivity filter of the cation channel TRPM4. *J Biol Chem* 280, 22899-22906.

Nilius, B., Vennekens, R., Prenen, J., Hoenderop, J.G., Droogmans, G., and Bindels, R.J. (2001). The single pore residue Asp542 determines Ca²⁺ permeation and Mg²⁺ block of the epithelial Ca²⁺ channel. *J Biol Chem* 276, 1020-1025.

Oseguera, A.J., Islas, L.D., Garcia-Villegas, R., and Rosenbaum, T. (2007). On the mechanism of TBA block of the TRPV1 channel. *Biophys J* 92, 3901-3914.

Owsianik, G., Talavera, K., Voets, T., and Nilius, B. (2006). Permeation and selectivity of TRP channels. *Annu Rev Physiol* 68, 685-717.

Palovcak, E., Delemotte, L., Klein, M.L., and Carnevale, V. (2015). Comparative sequence analysis suggests a conserved gating mechanism for TRP channels. *J Gen Physiol* 146, 37-50.

Pan, J., Chen, Q., Willenbring, D., Yoshida, K., Tillman, T., Kashlan, O.B., Cohen, A., Kong, X.P., Xu, Y., and Tang, P. (2012). Structure of the pentameric ligand-gated ion channel ELIC cocrystallized with its competitive antagonist acetylcholine. *Nat Commun* 3, 714.

Pandit, S.B., and Skolnick, J. (2008). Fr-TM-align: a new protein structural alignment method based on fragment alignments and the TM-score. *BMC Bioinformatics* 9, 531.

Paulsen, C.E., Armache, J.P., Gao, Y., Cheng, Y., and Julius, D. (2015). Structure of the TRPA1 ion channel suggests regulatory mechanisms. *Nature* 525, 552.

Premkumar, L.S., Agarwal, S., and Steffen, D. (2002). Single-channel properties of native and cloned rat vanilloid receptors. *J Physiol* 545, 107-117.

Pumroy, R.A., Samanta, A., Liu, Y., Hughes, T.E., Zhao, S., Yudin, Y., Rohacs, T., Han, S., and Moiseenkova-Bell, V.Y. (2019). Molecular mechanism of TRPV2 channel modulation by cannabidiol. *Elife* 8.

Qin, N., Neeper, M.P., Liu, Y., Hutchinson, T.L., Lubin, M.L., and Flores, C.M. (2008). TRPV2 is activated by cannabidiol and mediates CGRP release in cultured rat dorsal root ganglion neurons. *J Neurosci* 28, 6231-6238.

Ramsey, I.S., Delling, M., and Clapham, D.E. (2006). An introduction to TRP channels. *Annu Rev Physiol* 68, 619-647.

Riek, R.P., and Graham, R.M. (2011). The elusive pi-helix. *J Struct Biol* 173, 153-160.

Riek, R.P., Rigoutsos, I., Novotny, J., and Graham, R.M. (2001). Non-alpha-helical elements modulate polytopic membrane protein architecture. *J Mol Biol* 306, 349-362.

Ross, H.R., Napier, I., and Connor, M. (2008). Inhibition of recombinant human T-type calcium channels by Delta9-tetrahydrocannabinol and cannabidiol. *J Biol Chem* 283, 16124-16134.

Salazar, H., Jara-Oseguera, A., Hernandez-Garcia, E., Llorente, I., Arias, O., II, Soriano-Garcia, M., Islas, L.D., and Rosenbaum, T. (2009). Structural determinants of gating in the TRPV1 channel. *Nat Struct Mol Biol* 16, 704-710.

Saotome, K., Singh, A.K., Yelshanskaya, M.V., and Sobolevsky, A.I. (2016). Crystal structure of the epithelial calcium channel TRPV6. *Nature* 534, 506-511.

Sarkar, D., Singh, Y., and Kalia, J. (2018). Protein-Lipid Interfaces Can Drive the Functions of Membrane-Embedded Protein-Protein Complexes. *ACS chemical biology* 13, 2689-2698.

Schmiege, P., Fine, M., Blobel, G., and Li, X. (2017). Human TRPML1 channel structures in open and closed conformations. *Nature* 550, 366-370.

Schrödinger, L. (2015). The {PyMOL} Molecular Graphics System, Version~1.8.

Shen, P.S., Yang, X., DeCaen, P.G., Liu, X., Bulkley, D., Clapham, D.E., and Cao, E. (2016). The Structure of the Polycystic Kidney Disease Channel PKD2 in Lipid Nanodiscs. *Cell* 167, 763-773 e711.

Singh, A.K., McGoldrick, L.L., Demirkhanyan, L., Leslie, M., Zakharian, E., and Sobolevsky, A.I. (2019). Structural basis of temperature sensation by the TRP channel TRPV3. *Nat Struct Mol Biol* 26, 994-998.

Singh, A.K., McGoldrick, L.L., and Sobolevsky, A.I. (2018a). Structure and gating mechanism of the transient receptor potential channel TRPV3. *Nat Struct Mol Biol* 25, 805-813.

Singh, A.K., McGoldrick, L.L., Twomey, E.C., and Sobolevsky, A.I. (2018b). Mechanism of calmodulin inactivation of the calcium-selective TRP channel TRPV6. *Sci Adv* 4, eaau6088.

Singh, A.K., Saotome, K., McGoldrick, L.L., and Sobolevsky, A.I. (2018c). Structural bases of TRP channel TRPV6 allosteric modulation by 2-APB. *Nat Commun* 9, 2465.

Singh, A.K., Saotome, K., and Sobolevsky, A.I. (2017). Swapping of transmembrane domains in the epithelial calcium channel TRPV6. *Scientific reports* 7, 10669.

Smart, O.S., Neduelil, J.G., Wang, X., Wallace, B.A., and Sansom, M.S. (1996). HOLE: a program for the analysis of the pore dimensions of ion channel structural models. *J Mol Graph* 14, 354-360, 376.

Stamm, M., and Forrest, L.R. (2015). Structure alignment of membrane proteins: Accuracy of available tools and a consensus strategy. *Proteins: Structure, Function, and Bioinformatics* 83, 1720-1732.

Su, Q., Hu, F., Ge, X., Lei, J., Yu, S., Wang, T., Zhou, Q., Mei, C., and Shi, Y. (2018a). Structure of the human PKD1-PKD2 complex. *Science* 361.

Su, Q., Hu, F., Liu, Y., Ge, X., Mei, C., Yu, S., Shen, A., Zhou, Q., Yan, C., Lei, J., *et al.* (2018b). Cryo-EM structure of the polycystic kidney disease-like channel PKD2L1. *Nat Commun* 9, 1192.

Sun, J., and MacKinnon, R. (2020). Structural Basis of Human KCNQ1 Modulation and Gating. *Cell* 180, 340-347 e349.

Tang, Q., Guo, W., Zheng, L., Wu, J.X., Liu, M., Zhou, X., Zhang, X., and Chen, L. (2018). Structure of the receptor-activated human TRPC6 and TRPC3 ion channels. *Cell research* 28, 746-755.

Tao, X., Hite, R.K., and MacKinnon, R. (2017). Cryo-EM structure of the open high-conductance Ca(2+)-activated K(+) channel. *Nature* 541, 46-51.

Tao, X., and MacKinnon, R. (2019a). Cryo-EM structure of the KvAP channel reveals a non-domain-swapped voltage sensor topology. *Elife* 8.

Tao, X., and MacKinnon, R. (2019b). Molecular structures of the human Slo1 K(+) channel in complex with beta4. *Elife* 8.

Thompson, C.H., and Kearney, J.A. (2016). Cannabidiol Mellows Out Resurgent Sodium Current. *Epilepsy Curr* 16, 399-401.

Togashi, K., Inada, H., and Tominaga, M. (2008). Inhibition of the transient receptor potential cation channel TRPM2 by 2-aminoethoxydiphenyl borate (2-APB). *Br J Pharmacol* 153, 1324-1330.

Touw, W.G., Baakman, C., Black, J., te Beek, T.A.H., Krieger, E., Joosten, R.P., and Vriend, G. (2015). A series of PDB-related databanks for everyday needs. *Nucleic acids research* 43, D364-D368.

Venkatachalam, K., and Montell, C. (2007). TRP channels. *Annu Rev Biochem* 76, 387-417.

Vinayagam, D., Mager, T., Apelbaum, A., Bothe, A., Merino, F., Hofnagel, O., Gatsogiannis, C., and Raunser, S. (2018). Electron cryo-microscopy structure of the canonical TRPC4 ion channel. *eLife* 7, e36615.

Virtanen, P., Gommers, R., Oliphant, T.E., Haberland, M., Reddy, T., Cournapeau, D., Burovski, E., Peterson, P., Weckesser, W., Bright, J., *et al.* (2020). Author Correction: SciPy 1.0: fundamental algorithms for scientific computing in Python. *Nature Methods* 17, 352-352.

Voets, T., Prenen, J., Vriens, J., Watanabe, H., Janssens, A., Wissenbach, U., Boddling, M., Droogmans, G., and Nilius, B. (2002). Molecular determinants of permeation through the cation channel TRPV4. *J Biol Chem* 277, 33704-33710.

Wang, L., Fu, T.M., Zhou, Y., Xia, S., Greka, A., and Wu, H. (2018). Structures and gating mechanism of human TRPM2. *Science* 362.

Wang, W., and MacKinnon, R. (2017). Cryo-EM Structure of the Open Human Ether-a-go-go-Related K(+) Channel hERG. *Cell* 169, 422-430 e410.

Waskom, M., Botvinnik, O., O'Kane, D., Hobson, P., Ostblom, J., Lukauskas, S., Gemperline, D.C., Augspurger, T., Halchenko, Y., Cole, J.B., *et al.* (2018). mwaskom/seaborn: v0.9.0 (July 2018) (Zenodo).

Waterhouse, A.M., Procter, J.B., Martin, D.M.A., Clamp, M., and Barton, G.J. (2009). Jalview Version 2—a multiple sequence alignment editor and analysis workbench. *Bioinformatics* 25, 1189-1191.

Weil, A., Moore, S.E., Waite, N.J., Randall, A., and Gunthorpe, M.J. (2005). Conservation of functional and pharmacological properties in the distantly related temperature sensors TRPV1 and TRPM8. *Mol Pharmacol* 68, 518-527.

Whorton, M.R., and MacKinnon, R. (2013). X-ray structure of the mammalian GIRK2-beta gamma G-protein complex. *Nature* 498, 190-197.

Wilkes, M., Madej, M.G., Kreuter, L., Rhinow, D., Heinz, V., De Sanctis, S., Ruppel, S., Richter, R.M., Joos, F., Grieben, M., *et al.* (2017). Molecular insights into lipid-assisted Ca(2+) regulation of the TRP channel Polycystin-2. *Nat Struct Mol Biol* 24, 123-130.

Winkler, P.A., Huang, Y., Sun, W., Du, J., and Lu, W. (2017). Electron cryo-microscopy structure of a human TRPM4 channel. *Nature* 552, 200-204.

Xu, J., and Zhang, Y. (2010). How significant is a protein structure similarity with TM-score = 0.5? *Bioinformatics* 26, 889-895.

Xu, S.-Z., Zeng, F., Boulay, G., Grimm, C., Harteneck, C., and Beech, D.J. (2005). Block of TRPC5 channels by 2-aminoethoxydiphenyl borate: a differential, extracellular and voltage-dependent effect. *Br J Pharmacol* 145, 405-414.

Yin, Y., Le, S.C., Hsu, A.L., Borgnia, M.J., Yang, H., and Lee, S.Y. (2019a). Structural basis of cooling agent and lipid sensing by the cold-activated TRPM8 channel. *Science (New York, NY)* 363.

Yin, Y., Wu, M., Hsu, A.L., Borschel, W.F., Borgnia, M.J., Lander, G.C., and Lee, S.Y. (2019b). Visualizing structural transitions of ligand-dependent gating of the TRPM2 channel. *Nat Commun* 10, 3740.

Yin, Y., Wu, M., Zubcevic, L., Borschel, W.F., Lander, G.C., and Lee, S.Y. (2018). Structure of the cold- and menthol-sensing ion channel TRPM8. *Science (New York, NY)* 359, 237-241.

Yu, F.H., and Catterall, W.A. (2004). The VGL-chanome: a protein superfamily specialized for electrical signaling and ionic homeostasis. *Sci STKE* 2004, re15.

Yudin, Y., and Rohacs, T. (2012). Regulation of TRPM8 channel activity. *Mol Cell Endocrinol* 353, 68-74.

Zakharian, E., Cao, C., and Rohacs, T. (2011). Intracellular ATP supports TRPV6 activity via lipid kinases and the generation of PtdIns(4,5) P(2). *FASEB J* 25, 3915-3928.

Zhang, F., Hanson, S.M., Jara-Oseguera, A., Krepiy, D., Bae, C., Pearce, L.V., Blumberg, P.M., Newstead, S., and Swartz, K.J. (2016). Engineering vanilloid-sensitivity into the rat TRPV2 channel. *Elife* 5.

Zhang, F., Swartz, K.J., and Jara-Oseguera, A. (2019). Conserved allosteric pathways for activation of TRPV3 revealed through engineering vanilloid-sensitivity. *Elife* 8.

Zhang, Y., and Skolnick, J. (2004). Scoring function for automated assessment of protein structure template quality. *Proteins: Structure, Function, and Bioinformatics* 57, 702-710.

Zhang, Y., and Skolnick, J. (2005). TM-align: a protein structure alignment algorithm based on the TM-score. *Nucleic Acids Res* 33, 2302-2309.

Zhang, Z., Toth, B., Szollosi, A., Chen, J., and Csanady, L. (2018a). Structure of a TRPM2 channel in complex with Ca(2+) explains unique gating regulation. *Elife* 7.

Zhang, Z., Tóth, B., Szollosi, A., Chen, J., and Csanády, L. (2018b). Structure of a TRPM2 channel in complex with Ca²⁺ explains unique gating regulation. *eLife* 7, e36409.

Zheng, W., Yang, X., Hu, R., Cai, R., Hofmann, L., Wang, Z., Hu, Q., Liu, X., Bulkley, D., Yu, Y., *et al.* (2018). Hydrophobic pore gates regulate ion permeation in polycystic kidney disease 2 and 2L1 channels. *Nat Commun* 9, 2302.

Zhou, X., Li, M., Su, D., Jia, Q., Li, H., Li, X., and Yang, J. (2017). Cryo-EM structures of the human endolysosomal TRPML3 channel in three distinct states. *Nat Struct Mol Biol* 24, 1146-1154.

Zhou, Y., Morais-Cabral, J.H., Kaufman, A., and MacKinnon, R. (2001). Chemistry of ion coordination and hydration revealed by a K⁺ channel- Fab complex at 2.0 Å resolution. *Nature* 414, 43-48.

Zubcevic, L., Borschel, W.F., Hsu, A.L., Borgnia, M.J., and Lee, S.Y. (2019a). Regulatory switch at the cytoplasmic interface controls TRPV channel gating. *Elife* 8.

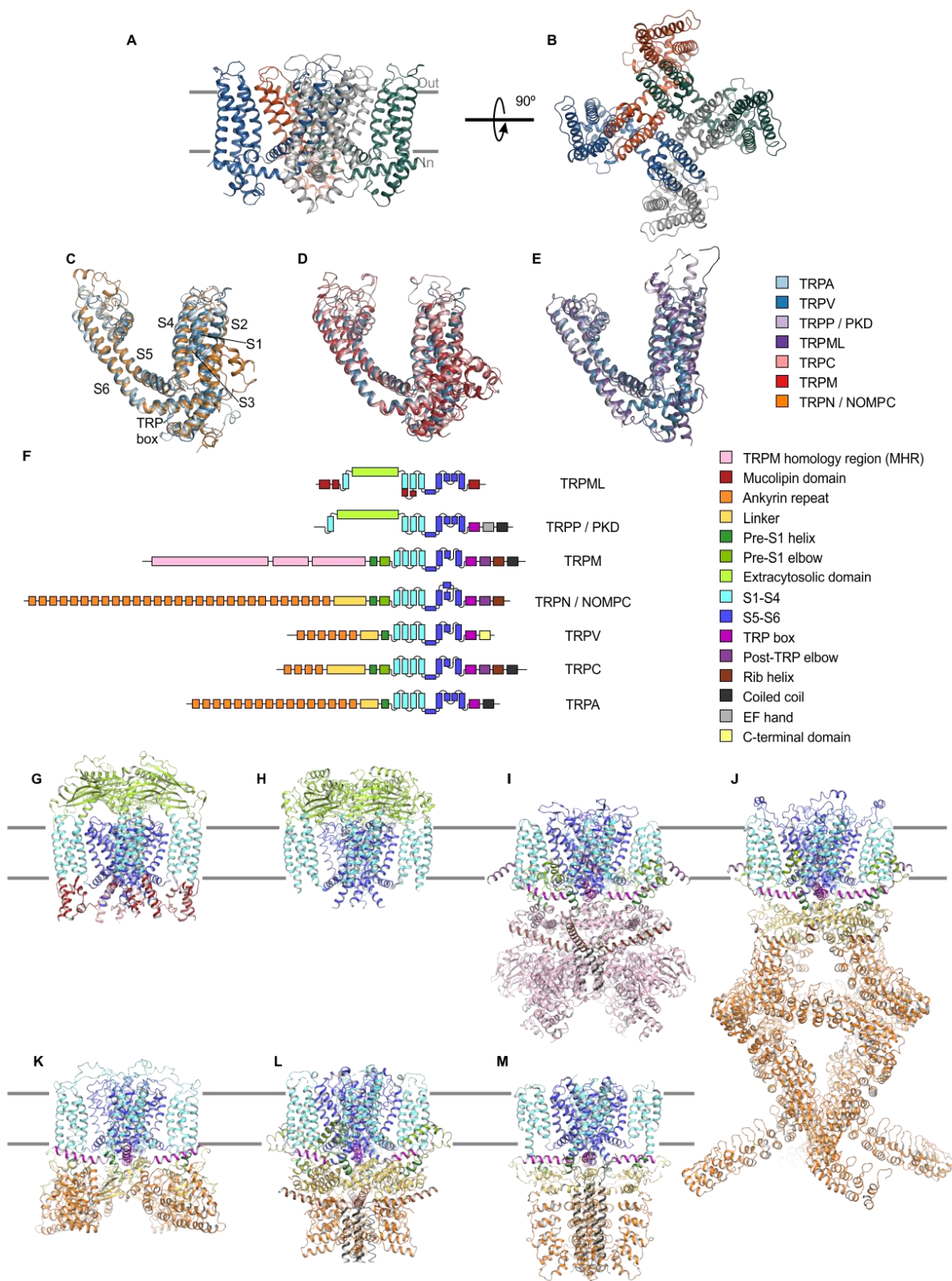
Zubcevic, L., Herzik, M.A., Jr., Chung, B.C., Liu, Z., Lander, G.C., and Lee, S.Y. (2016). Cryo-electron microscopy structure of the TRPV2 ion channel. *Nat Struct Mol Biol* 23, 180-186.

Zubcevic, L., Herzik, M.A., Jr., Wu, M., Borschel, W.F., Hirschi, M., Song, A.S., Lander, G.C., and Lee, S.Y. (2018a). Conformational ensemble of the human TRPV3 ion channel. *Nat Commun* 9, 4773.

Zubcevic, L., Hsu, A.L., Borgnia, M.J., and Lee, S.Y. (2019b). Symmetry transitions during gating of the TRPV2 ion channel in lipid membranes. *Elife* 8.

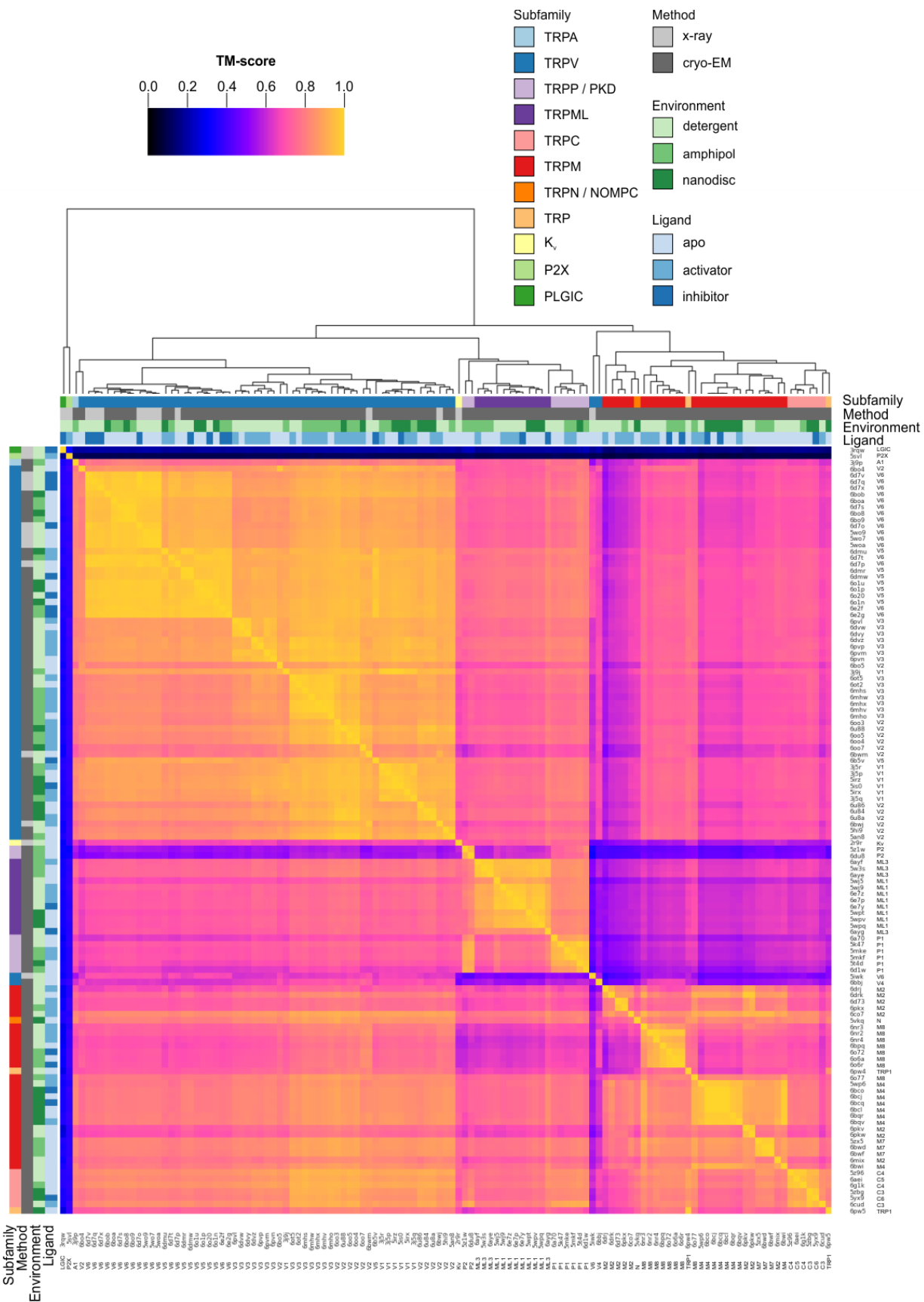
Zubcevic, L., Le, S., Yang, H., and Lee, S.Y. (2018b). Conformational plasticity in the selectivity filter of the TRPV2 ion channel. *Nat Struct Mol Biol* 25, 405-415.

Zubcevic, L., and Lee, S.Y. (2019). The role of pi-helices in TRP channel gating. *Curr Opin Struct Biol* 58, 314-323.



← **Figure 1. Structures of TRP channel subfamilies.**

(A) Backbone fold of apo TRPV1 in nanodiscs (5irz) viewed from the side, with approximate boundaries of the membrane indicated with gray bars. **(B)** Same structure as in A viewed from the extracellular side. **(C-E)** Superimposed structures of TM domains for apo TRPV1 (blue; 5irz) with **(C)** apo TRPN (orange; 5vkq) and apo TRPA1 (light blue; 3j9p), **(D)** apo TRPC5 (pink; 6aei) and apo TRPM4 (red; 6bcj). **(E)** apo TRPML3 (dark purple; 5w3s) and apo TRPP1 (light purple; 5t4d). For clarity, only one of the four subunits shown. **(F)** Schematic of domain architecture of TRP channel subunits. **(G-M)** Cartoon representation of structure with domains colored as in F of apo structures of **(G)** TRPML3 (5w3s), **(H)** TRPP1 (5t4d), **(I)** TRPM4 (6bcj), **(J)** TRPN (5vkq), **(K)** TRPV5 (6o1n), **(L)** TRPC5 (6aei), and **(M)** TRPA1 (3j9p).



← **Figure 2 Clustered heatmap of TM-scores for the pairwise structural alignments of the TM domains of TRP channels.**

The heatmap indicates how similar the TM domain (pre-S1 to TRP box) of each pair of TRP channel structures is, as expressed by the TM-score reported for each pairwise structural alignment performed with Fr-TM-align. A comparison of identical structures is indicated with yellow (TM-score of 1), whereas no structural similarity is indicated with black (TM-score of 0). The TM-score is further used to cluster the TRP channel structures. Representative Kv, P2X and PLGIC channel structures are included as a control. Note that the heatmap is not symmetric because the TM-score takes into account the sequence length of the reference structure (see Methods).

Figure 2 – Source Data 1 Master TRP channel list

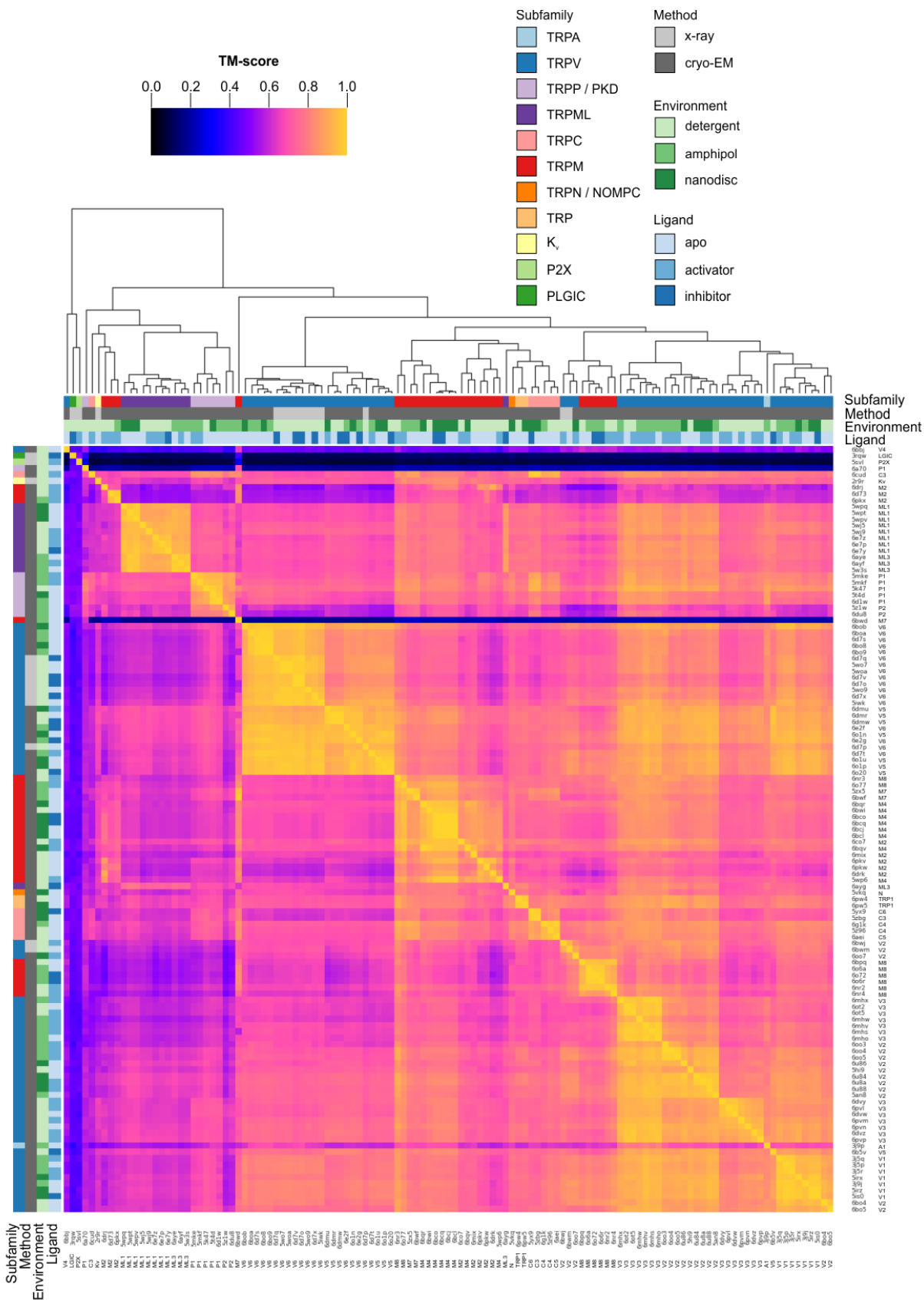
Figure 2 – Source Data 2 Data file for clustered heatmap of TM domain

Figure 2 – Source Data 3 Data file for clustered heatmap of pore domain

Figure 2 – Source Data 4 Data file for clustered heatmap of S1-S4 domain

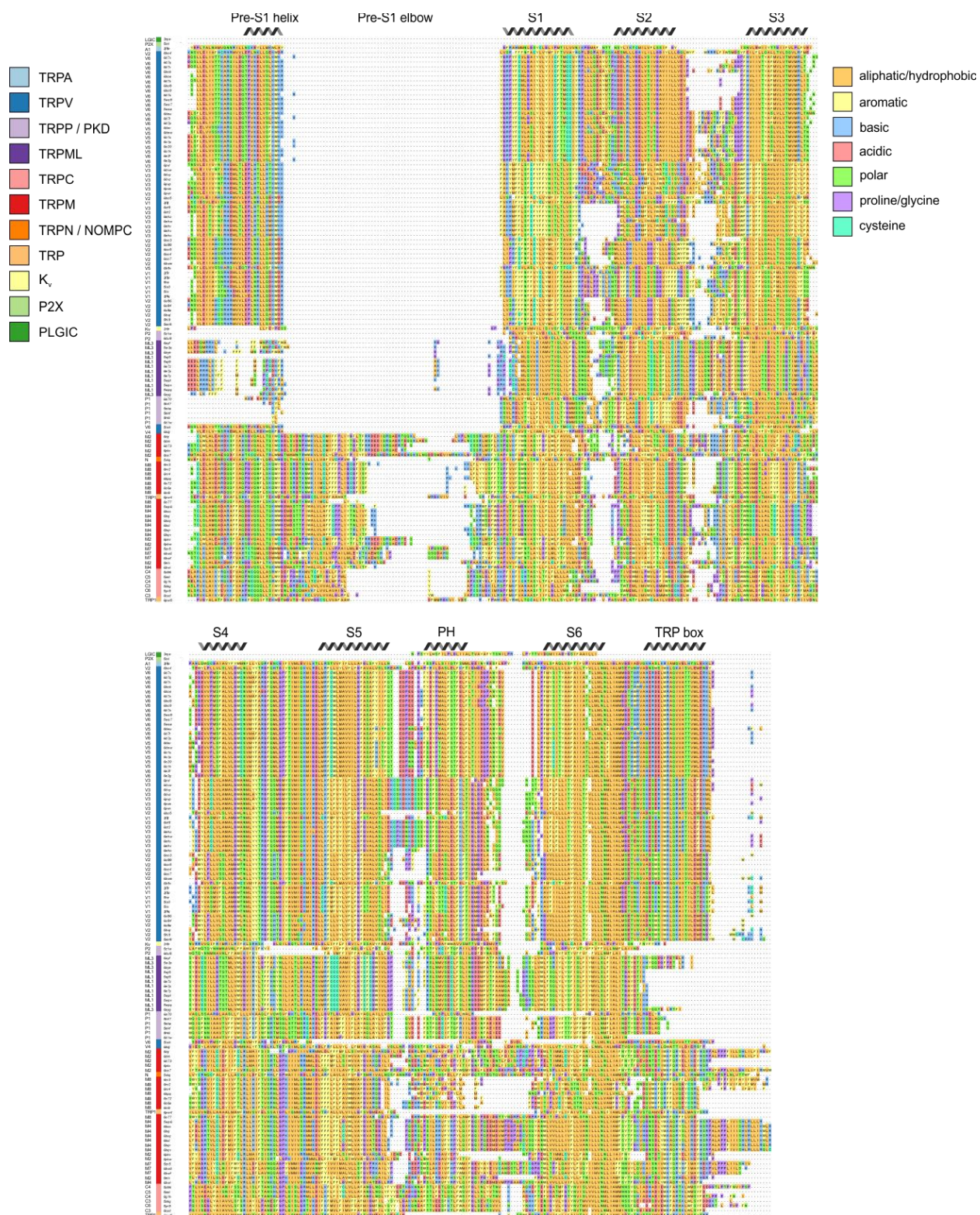
← **Figure 2 – Figure Supplement 1. Clustered heatmap of TM-scores for the pairwise structural alignments of the pore domains of TRP channels.**

The heatmap indicates how similar the pore domain (S5-S6) of each pair of TRP channel structures is, as expressed by the TM-score reported for each pairwise structural alignment performed with Fr-TM-align. A comparison of identical structures is indicated with yellow (TM-score of 1), whereas no structural similarity is indicated with black (TM-score of 0). The TM-score is further used to cluster the TRP channel structures. Representative Kv, P2X and PLGIC channel structures are included as a control. Note that the heatmap is not symmetric because the TM-score takes into account the sequence length of the reference structure (see Methods).



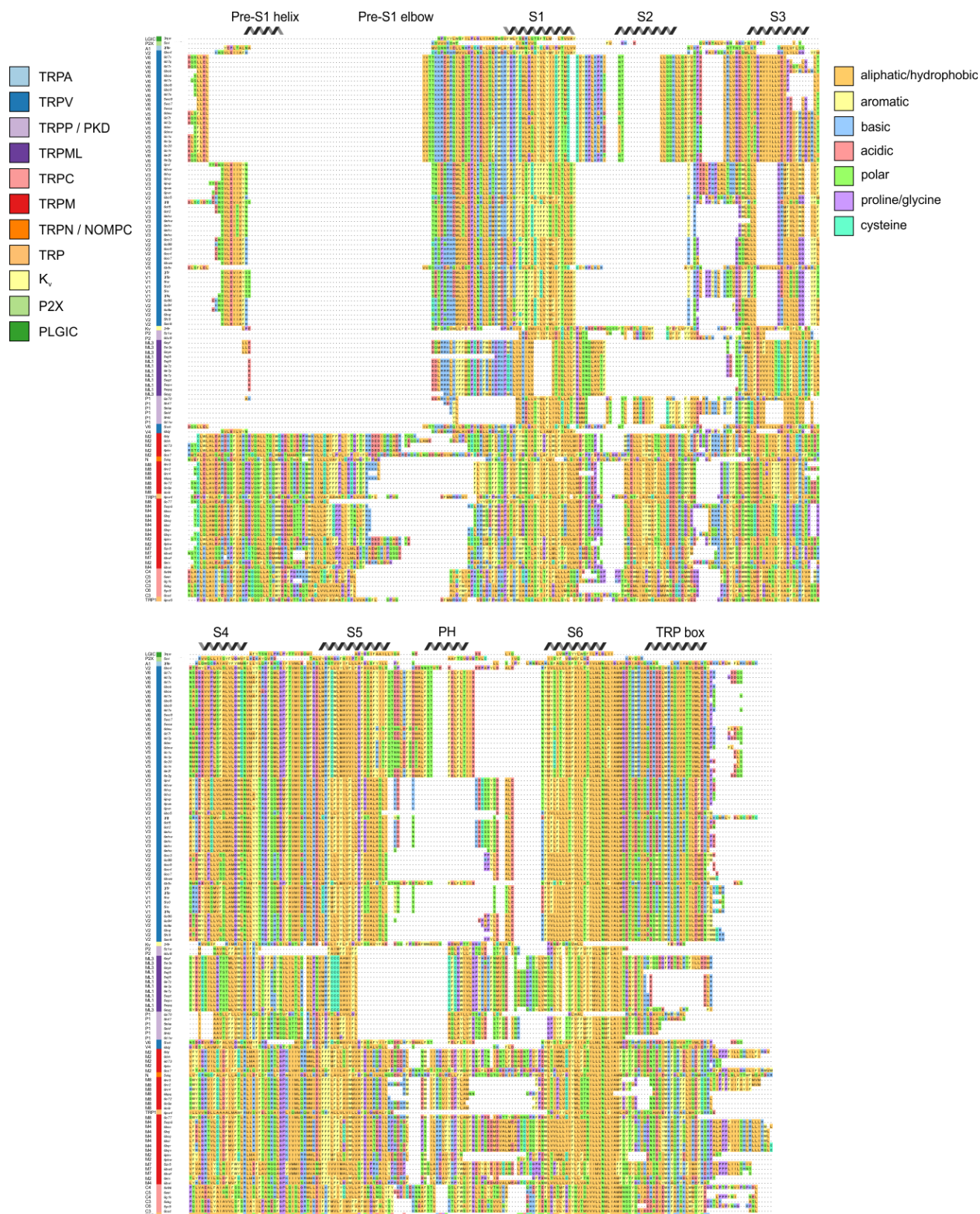
← **Figure 2 – Figure Supplement 2. Clustered heatmap of TM-scores for the pairwise structural alignments of the S1-S4 domains of TRP channels.**

The heatmap indicates how similar the S1-S4 domain of each pair of TRP channel structures is, as expressed by the TM-score reported for each pairwise structural alignment performed with Fr-TM-align. A comparison of identical structures is indicated with yellow (TM-score of 1), whereas no structural similarity is indicated with black (TM-score of 0). The TM-score is further used to cluster the TRP channel structures. Representative Kv, P2X and PLGIC channel structures are included as a control. Note that the heatmap is not symmetric because the TM-score takes into account the sequence length of the reference structure (see Methods).



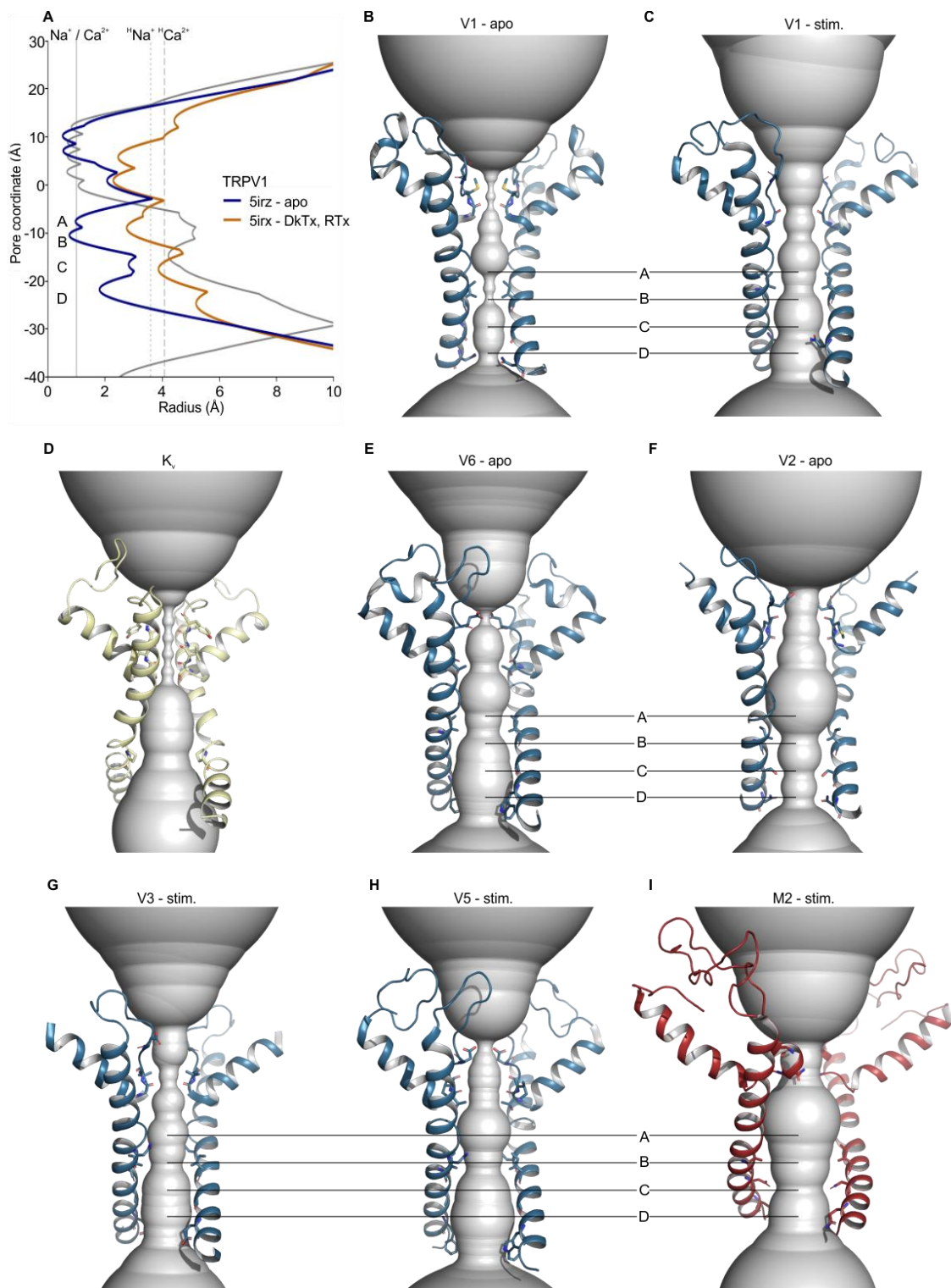
← Figure 2 – Figure Supplement 3. Structure-based multiple sequence alignment for TRP channels structures.

Structure-based multiple sequence alignment generated from Fr-TM-Align pairwise alignments of each structure with 6co7 as the template, omitting any residue that did not align to a residue in 6co7. Sequences are ordered based on hierarchical clustering from Figure 2. This sequence alignment shows the bounds of what was considered part of the TM domain, spanning from the pre-S1 helix to the TRP box. All domains are labeled based on structural consensus. PH stands for pore helix.



← Figure 2 – Figure Supplement 4. Multiple sequence alignment for TRP channel sequences whose structures have been determined and used for structure-based alignment.

Sequence-based multiple sequence alignment generated from ClustalOmega alignment of amino acid sequences from every determined structure, omitting any residue that did not align to a residue in 6co7. Sequences are ordered based on hierarchical clustering from Figure 2. All domains are labeled based on reference structure (6co7). PH stands for pore helix.



← **Figure 3. Pore radii in the S5-S6 pore domains of selected TRP channels according to HOLE.**

(A) Pore radius profiles for TRPV1 apo (blue, 5irz) and RTx/DkTx complex (orange, 5irx) structures and for the Kv1.2/2.1 paddle chimera (grey, 2r9r). Vertical lines indicate radii of dehydrated Na⁺ and Ca²⁺ ions (solid), hydrated Na⁺ (dotted, ^HNa⁺) and Ca²⁺ ions (dashed, ^HCa²⁺). (B-I) Backbones of tetrameric cation channel pore domains, focusing on structures with the widest S6 gate radii, with HOLE representations in gray for (B) apo TRPV1 (5irz), (C) TRPV1 with RTx/DkTx bound (5irx), (D) Kv 1.2/2.1 paddle chimera (2r9r), (E) apo TRPV6 (6bo9), (F) apo TRPV2 (6bo4), (G) TRPV3 Y564A mutant after pretreatment at 37 ° C (6pvp), (H) TRPV5 with PIP₂ (6dmu), and (I) TRPM2 with Ca²⁺ and ADP-ribose (6drj).

Figure 3 – Source Data 1 **Data file containing HOLE profile analysis for TRP channel pore domains.**

Figure 3 – Source Data 2 **Data file for minimum SF and S6 radii scatterplot**

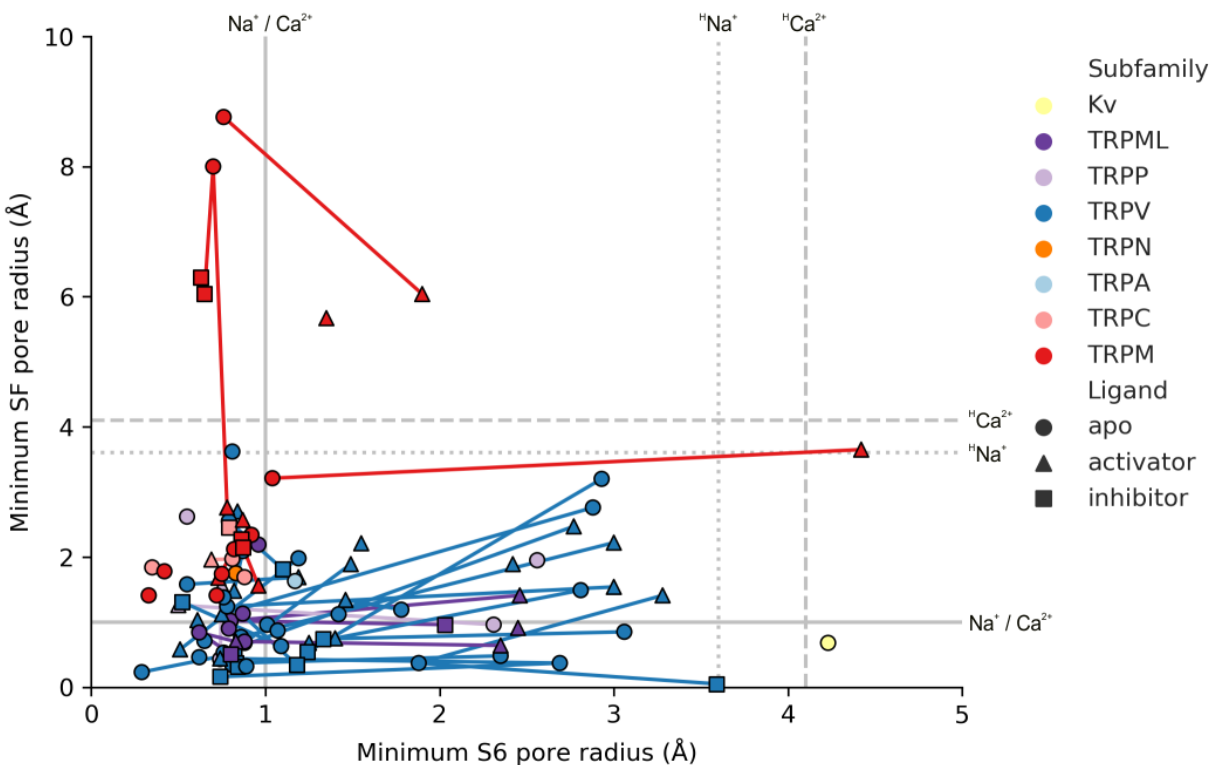
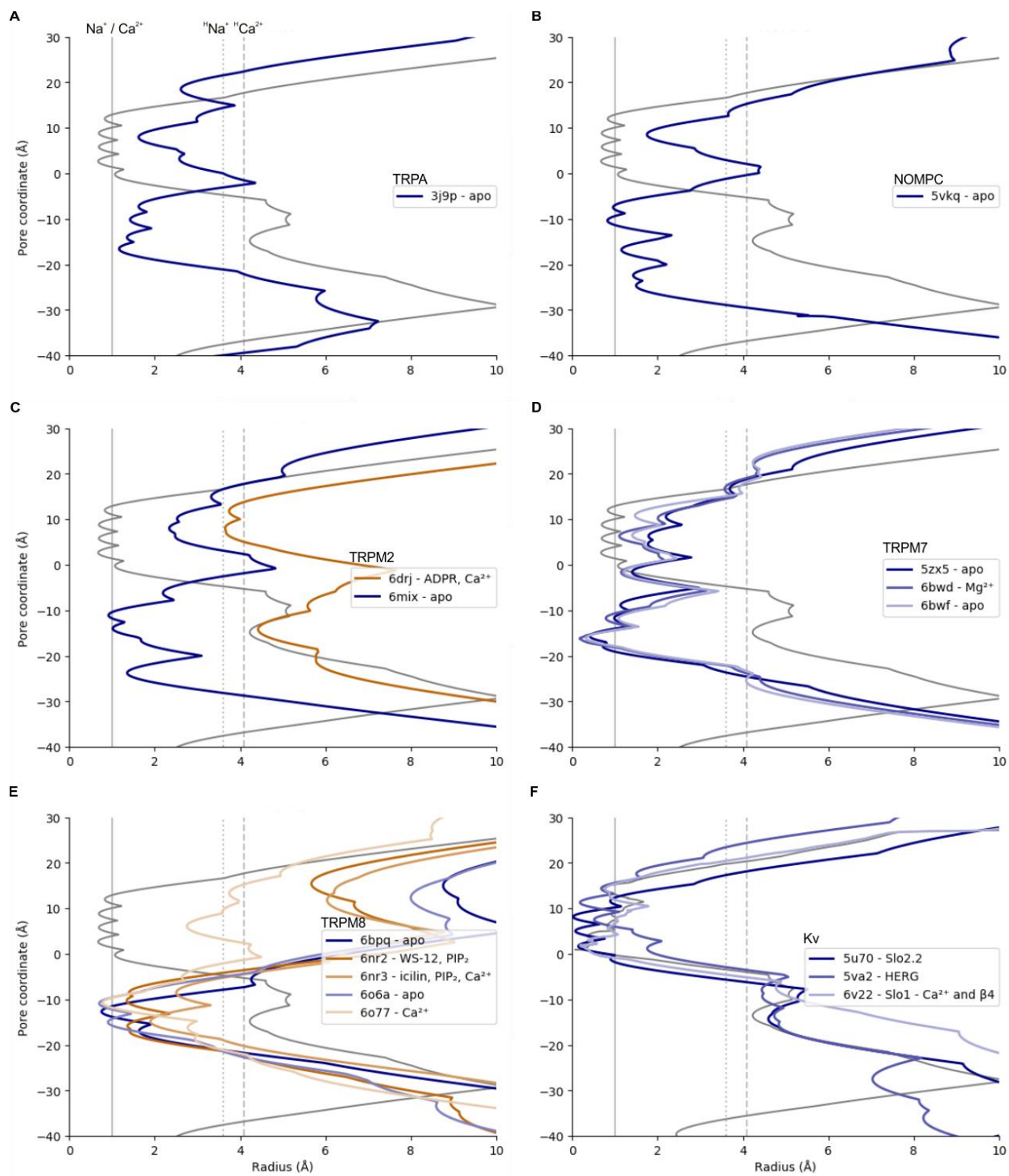


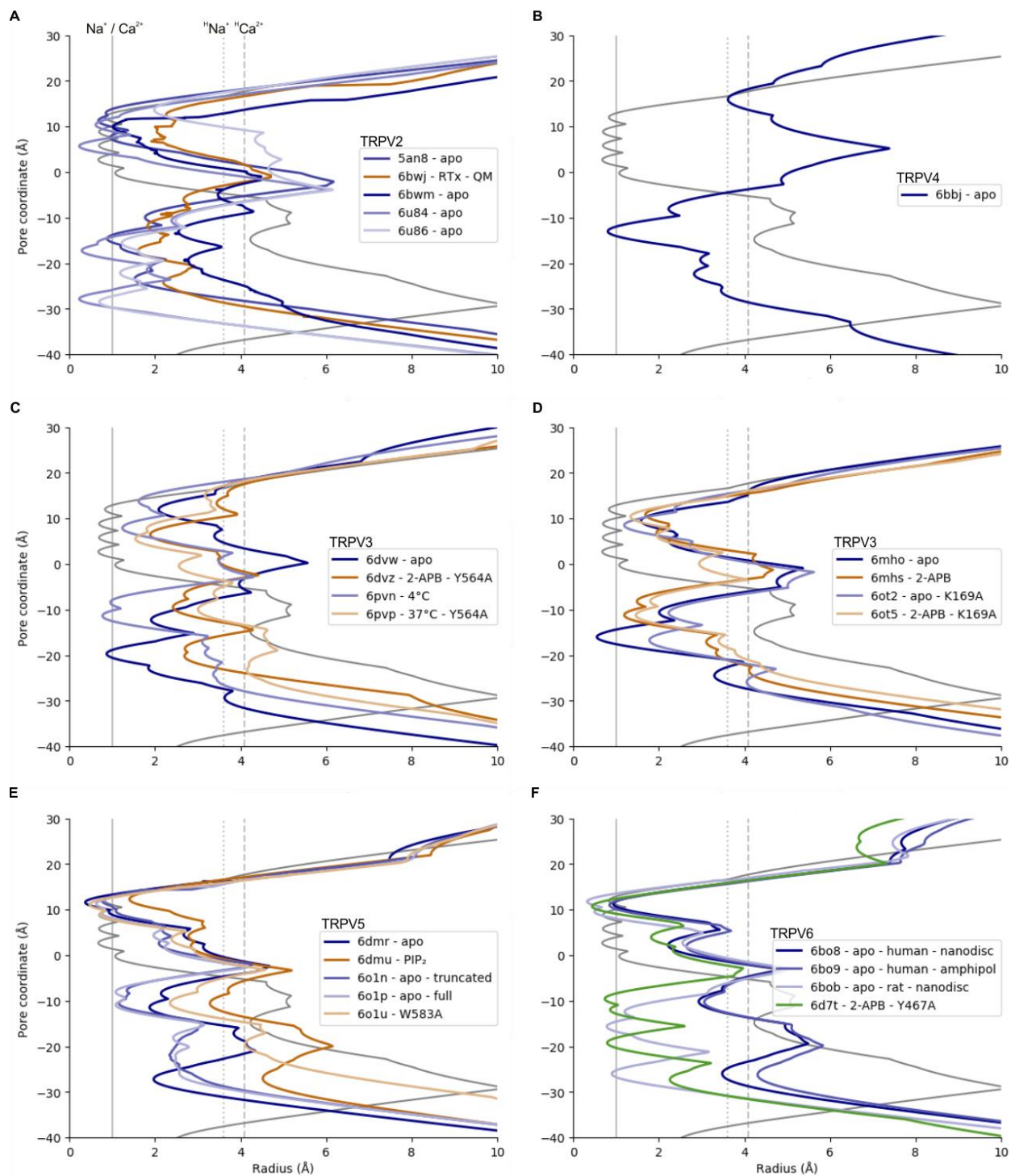
Figure 3 – Figure Supplement 1. Comparing selectivity filter and internal pore minimum radii for TRP channel structures.

The narrowest pore radius formed by the selectivity filter (SF) is plotted against the narrowest pore radius found at the internal end of S6. Each marker represents one structure. Markers that represent the same channel determined under different conditions to obtain different conformations are connected with lines. Grey lines represent radii of dehydrated Na⁺ and Ca²⁺ ions (solid), hydrated Na⁺ (dotted, ^HNa⁺) and hydrated Ca²⁺ ions (dashed, ^HCa²⁺).



← **Figure 3 – Figure Supplement 2. HOLE pore radius representations for S5-S6 pore domains of representative TRP and Kv channels.**

Pore radius profiles for TRP channel structures and for the Kv1.2/2.1 paddle chimera (grey, 2r9r). Vertical lines indicate radii of dehydrated Na⁺ and Ca²⁺ ions (solid), hydrated Na⁺ (dotted, ^HNa⁺) and Ca²⁺ ions (dashed, ^HCa²⁺). Profiles are shown for structures of (A) TRPA1, (B) NOMPC, (C) TRPM2, (D) TRPM7, (E) TRPM8, and (F) Kv. Where applicable, apo structure profiles are shown in blue and activator-bound structure profiles are shown in orange. Note that for TRPM8 structures shown, only 6o77 has sufficient resolution in the extracellular selectivity filter.



← **Figure 3 – Figure Supplement 3. HOLE pore radius representations for S5-S6 pore domains of representative TRP channels.**

Pore radius profiles for TRP channel structures and for the Kv1.2/2.1 paddle chimera (grey, 2r9r). Vertical lines indicate radii of dehydrated Na⁺ and Ca²⁺ ions (solid), hydrated Na⁺ (dotted, ^HNa⁺) and Ca²⁺ ions (dashed, ^HCa²⁺). Profiles are shown for structures of **(A)** TRPV2, **(B)** TRPV4, **(C,D)** TRPV3, **(E)** TRPV5, and **(F)** TRPV6. Where applicable, apo structure profiles are shown in blue, activator-bound structure profiles are shown in orange, and inhibitor-bound structure profiles are shown in green.

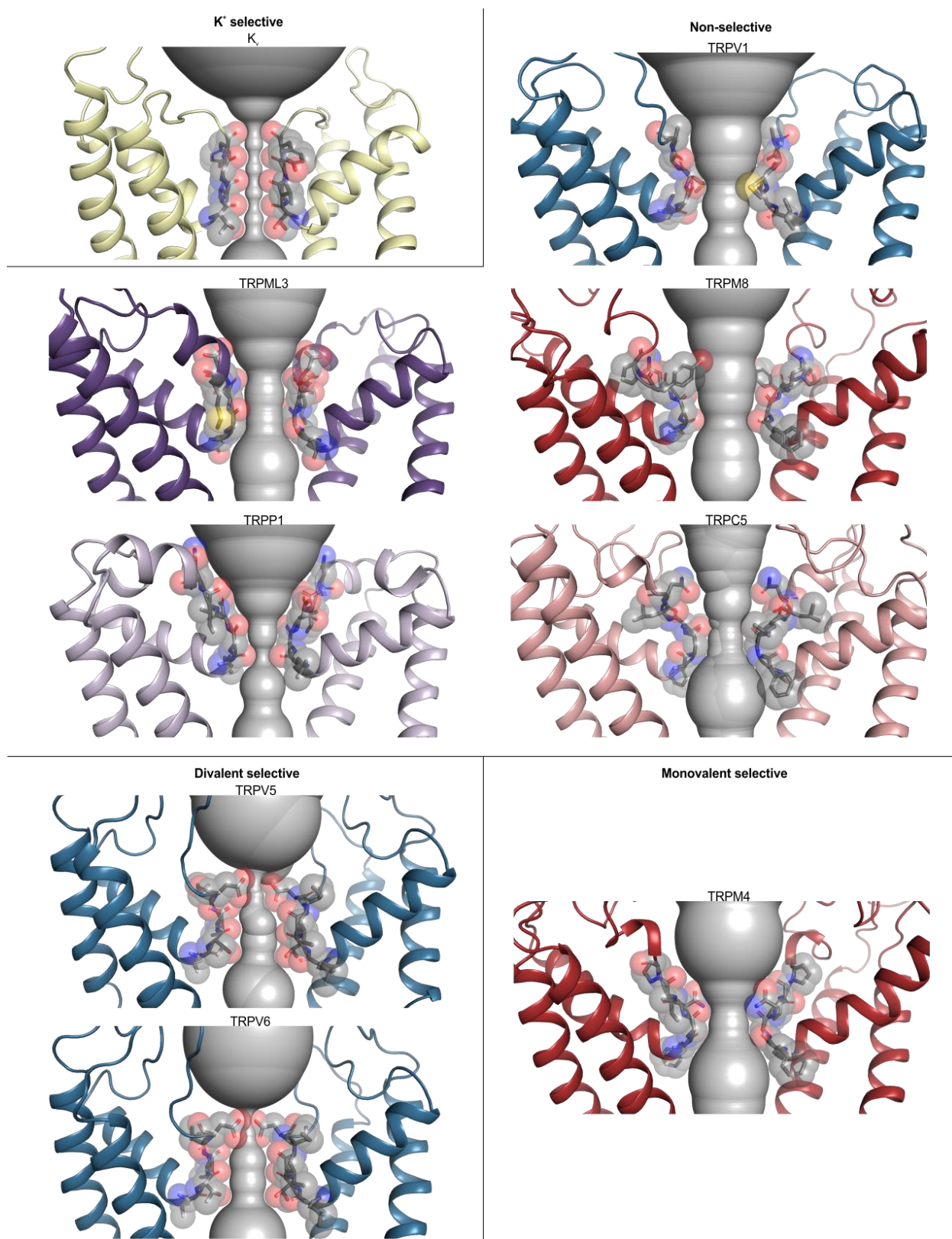
← **Figure 4 Structure-based multiple sequence alignment of pore-lining residues**

Structure-based multiple sequence alignment of pore-lining residues, with pore-contributing residues colored based on the narrowest pore radius associated with any atom in that residue (from magenta for narrowest to green for widest, passing through gold at 4.1 Å to represent the radius of a hydrated Ca²⁺ ion). Uncolored residues do not have any atoms whose van der Waals radii intersect with the HOLE profile. Sequences are ordered based on hierarchical clustering from Figure 2. The selectivity filter is indicated by SF.

← Figure 4 – Figure Supplement 1. Structure-based multiple sequence alignment of pore-lining residues.

Structure-based multiple sequence alignment of pore-lining residues, with all residues colored based on side chain character. Sequences are ordered based on hierarchical clustering from Figure 2. The selectivity filter is indicated by SF.

Figure 4 – Source Data 1 **Excel file**



← **Figure 5 Selectivity filters in TRP channels with different ion selectivity**

Pore domains (S5-S6) of selected TRP channels, focusing on the selectivity filter constriction at the extracellular end of the pore. Residues lining the selectivity filter are shown as grey sticks and spheres, with HOLE profiles shown as grey spheres. PDB accession codes are 2r9r (Kv 1.2/2.1 paddle chimera), 5irx (TRPV1), 5w3s (TRPML3), 6o77 (TRPM8), 5t4d (TRPP1), 6aei (TRPC5), 6o1n (TRPV5), 5iwk (TRPV6), and 6bco (TRPM4). While TRPM5 is also classified as monovalent-selective, due to lack of available structures, this channel is not represented in the figure.

← **Figure 6 Heatmaps comparing ligand binding pocket motifs in TRP channels**

Ligand binding motifs were identified as including any residues with a side chain within 4 Å of the ligand. Heatmaps comparing the ligand binding motifs in all structures based on percent identity (0-100, white to blue) or similarity (0-100, white to orange) when compared to the reference ligand binding motif indicated with the letter R. Additional structures in which the ligand is also found are indicated with S (for secondary). Ligand-protein interactions are shown in Figure 7, Figure 8, Figure 9, and Figure 9 – Figure Supp. 1. Sequences are ordered based on hierarchical clustering from Figure 2. Color code for TRP channels is from Figure 2.

Figure 6 – Source Data 1. Ligand motif identity heatmap data.

Figure 6 – Source Data 2. Ligand motif similarity heatmap data.

← Figure 6 – Figure Supplement 1. Multiple sequence alignments for ligand binding pocket motifs in TRP channels.

Ligand binding motifs were identified as including any residues with a side chain within 4 Å of the ligand. Equivalent ligand binding motifs for each structure identified based on alignment with the ligand binding motif from the parent ligand-bound structure. The reference ligand-bound structures are highlighted with black boxes, and secondary ligand-bound structures are highlighted with grey boxes. Ligand binding locations are shown in Figure 7 and Figure 8. Sequences are ordered based on hierarchical clustering from Figure 2. Color coding for TRP channels (left) and for side-chain character are from Figure 4 – Figure Supp. 1.

LGIC	2-APB (V3, site 1)	2-APB (V3, site 2)	2-APB (V3, site 3)	2-APB (V6, site 2)	CBD	ML-SA1
P2X	3qiw	3qiw	3qiw	3qiw	3qiw	3qiw
A1	3p3b	3p3b	3p3b	3p3b	3p3b	3p3b
V6	6d7v	6d7v	6d7v	6d7v	6d7v	6d7v
V6	6d7g	6d7g	6d7g	6d7g	6d7g	6d7g
V6	6d7x	6d7x	6d7x	6d7x	6d7x	6d7x
V6	6b0a	6b0a	6b0a	6b0a	6b0a	6b0a
V6	6d7a	6d7a	6d7a	6d7a	6d7a	6d7a
V6	6b08	6b08	6b08	6b08	6b08	6b08
V6	6b09	6b09	6b09	6b09	6b09	6b09
V6	6d7o	6d7o	6d7o	6d7o	6d7o	6d7o
V6	5w09	5w09	5w09	5w09	5w09	5w09
V6	5w07	5w07	5w07	5w07	5w07	5w07
V6	5w0a	5w0a	5w0a	5w0a	5w0a	5w0a
V5	6dnu	6dnu	6dnu	6dnu	6dnu	6dnu
V6	6d7t	6d7t	6d7t	6d7t	6d7t	6d7t
V6	6d7p	6d7p	6d7p	6d7p	6d7p	6d7p
V5	6dnuw	6dnuw	6dnuw	6dnuw	6dnuw	6dnuw
V5	6o1u	6o1u	6o1u	6o1u	6o1u	6o1u
V5	6o1p	6o1p	6o1p	6o1p	6o1p	6o1p
V5	6o20	6o20	6o20	6o20	6o20	6o20
V5	6o1n	6o1n	6o1n	6o1n	6o1n	6o1n
V6	6e2f	6e2f	6e2f	6e2f	6e2f	6e2f
V6	6e2y	6e2y	6e2y	6e2y	6e2y	6e2y
V3	6pvl	6pvl	6pvl	6pvl	6pvl	6pvl
V3	6dvw	6dvw	6dvw	6dvw	6dvw	6dvw
V3	6dvy	6dvy	6dvy	6dvy	6dvy	6dvy
V3	6d7z	6d7z	6d7z	6d7z	6d7z	6d7z
V3	6pvm	6pvm	6pvm	6pvm	6pvm	6pvm
V3	6pvn	6pvn	6pvn	6pvn	6pvn	6pvn
V2	6b05	6b05	6b05	6b05	6b05	6b05
V1	3f9	3f9	3f9	3f9	3f9	3f9
V3	6d05	6d05	6d05	6d05	6d05	6d05
V3	6d02	6d02	6d02	6d02	6d02	6d02
V3	6e1z	6e1z	6e1z	6e1z	6e1z	6e1z
V3	6e1w	6e1w	6e1w	6e1w	6e1w	6e1w
V3	6e1x	6e1x	6e1x	6e1x	6e1x	6e1x
V3	6e1v	6e1v	6e1v	6e1v	6e1v	6e1v
V3	6e1h	6e1h	6e1h	6e1h	6e1h	6e1h
V2	6b03	6b03	6b03	6b03	6b03	6b03
V2	6u88	6u88	6u88	6u88	6u88	6u88
V2	6b05	6b05	6b05	6b05	6b05	6b05
V2	6b04	6b04	6b04	6b04	6b04	6b04
V2	6b07	6b07	6b07	6b07	6b07	6b07
V2	6b0w	6b0w	6b0w	6b0w	6b0w	6b0w
V5	6b5v	6b5v	6b5v	6b5v	6b5v	6b5v
V1	3f5	3f5	3f5	3f5	3f5	3f5
V1	3f0	3f0	3f0	3f0	3f0	3f0
V1	5r2	5r2	5r2	5r2	5r2	5r2
V1	5r0	5r0	5r0	5r0	5r0	5r0
V1	5r1	5r1	5r1	5r1	5r1	5r1
V1	3f5g	3f5g	3f5g	3f5g	3f5g	3f5g
V2	6u86	6u86	6u86	6u86	6u86	6u86
V2	6u84	6u84	6u84	6u84	6u84	6u84
V2	6u8a	6u8a	6u8a	6u8a	6u8a	6u8a
V2	6b0y	6b0y	6b0y	6b0y	6b0y	6b0y
V2	6b09	6b09	6b09	6b09	6b09	6b09
V2	5an8	5an8	5an8	5an8	5an8	5an8
Kv	2r9	2r9	2r9	2r9	2r9	2r9
P2	5c1w	5c1w	5c1w	5c1w	5c1w	5c1w
P2	6u8b	6u8b	6u8b	6u8b	6u8b	6u8b
ML3	6ayf	6ayf	6ayf	6ayf	6ayf	6ayf
ML3	5w3a	5w3a	5w3a	5w3a	5w3a	5w3a
ML3	6aye	6aye	6aye	6aye	6aye	6aye
ML1	5ug5	5ug5	5ug5	5ug5	5ug5	5ug5
ML1	5ug9	5ug9	5ug9	5ug9	5ug9	5ug9
ML1	6e7z	6e7z	6e7z	6e7z	6e7z	6e7z
ML1	6e7p	6e7p	6e7p	6e7p	6e7p	6e7p
ML1	6e7y	6e7y	6e7y	6e7y	6e7y	6e7y
ML1	5wpt	5wpt	5wpt	5wpt	5wpt	5wpt
ML1	5wvz	5wvz	5wvz	5wvz	5wvz	5wvz
ML1	5wvq	5wvq	5wvq	5wvq	5wvq	5wvq
ML3	6ayg	6ayg	6ayg	6ayg	6ayg	6ayg
P1	6a70	6a70	6a70	6a70	6a70	6a70
P1	5k47	5k47	5k47	5k47	5k47	5k47
P1	5e1e	5e1e	5e1e	5e1e	5e1e	5e1e
P1	5e1f	5e1f	5e1f	5e1f	5e1f	5e1f
P1	6d4f	6d4f	6d4f	6d4f	6d4f	6d4f
P1	6d1w	6d1w	6d1w	6d1w	6d1w	6d1w
V6	6w1k	6w1k	6w1k	6w1k	6w1k	6w1k
V4	6b1y	6b1y	6b1y	6b1y	6b1y	6b1y
M2	6d1g	6d1g	6d1g	6d1g	6d1g	6d1g
M2	6d1k	6d1k	6d1k	6d1k	6d1k	6d1k
M2	6d73	6d73	6d73	6d73	6d73	6d73
M2	6p1k	6p1k	6p1k	6p1k	6p1k	6p1k
M2	6e07	6e07	6e07	6e07	6e07	6e07
N	5v1q	5v1q	5v1q	5v1q	5v1q	5v1q
M8	6n3	6n3	6n3	6n3	6n3	6n3
M8	6n2	6n2	6n2	6n2	6n2	6n2
M8	6n4	6n4	6n4	6n4	6n4	6n4
M8	6b0q	6b0q	6b0q	6b0q	6b0q	6b0q
M8	6o72	6o72	6o72	6o72	6o72	6o72
M8	6o6a	6o6a	6o6a	6o6a	6o6a	6o6a
M8	6o6r	6o6r	6o6r	6o6r	6o6r	6o6r
TRP1	6p1v	6p1v	6p1v	6p1v	6p1v	6p1v
M4	6b07	6b07	6b07	6b07	6b07	6b07
M4	6b0c	6b0c	6b0c	6b0c	6b0c	6b0c
M4	6b0j	6b0j	6b0j	6b0j	6b0j	6b0j
M4	6b0q	6b0q	6b0q	6b0q	6b0q	6b0q
M4	6b0r	6b0r	6b0r	6b0r	6b0r	6b0r
M4	6b0v	6b0v	6b0v	6b0v	6b0v	6b0v
M2	6p1v	6p1v	6p1v	6p1v	6p1v	6p1v
M2	6p1w	6p1w	6p1w	6p1w	6p1w	6p1w
M7	6b0w	6b0w	6b0w	6b0w	6b0w	6b0w
M7	6b0f	6b0f	6b0f	6b0f	6b0f	6b0f
M2	6e1x	6e1x	6e1x	6e1x	6e1x	6e1x
M4	6b0y	6b0y	6b0y	6b0y	6b0y	6b0y
C4	6c96	6c96	6c96	6c96	6c96	6c96
C5	6e1f	6e1f	6e1f	6e1f	6e1f	6e1f
C4	6g1k	6g1k	6g1k	6g1k	6g1k	6g1k
C3	6c1b	6c1b	6c1b	6c1b	6c1b	6c1b
C6	6y19	6y19	6y19	6y19	6y19	6y19
C3	6c0d	6c0d	6c0d	6c0d	6c0d	6c0d
TRP1	6p1v5	6p1v5	6p1v5	6p1v5	6p1v5	6p1v5

← Figure 6 – Figure Supplement 2. Multiple sequence alignments for ligand binding pocket motifs in TRP channels.

Equivalent ligand binding motifs for each structure identified based on alignment with the ligand binding motif from the parent ligand-bound structure. The reference ligand-bound structures are highlighted with black boxes, and secondary ligand-bound structures are highlighted with grey boxes. Ligand binding locations are shown in Figure 9 and Figure 9 – Figure Supp. 1. Sequences are ordered based on hierarchical clustering from Figure 2. Color coding for TRP channels (left) and for side-chain character are from Figure 4 – Figure Supp. 1.

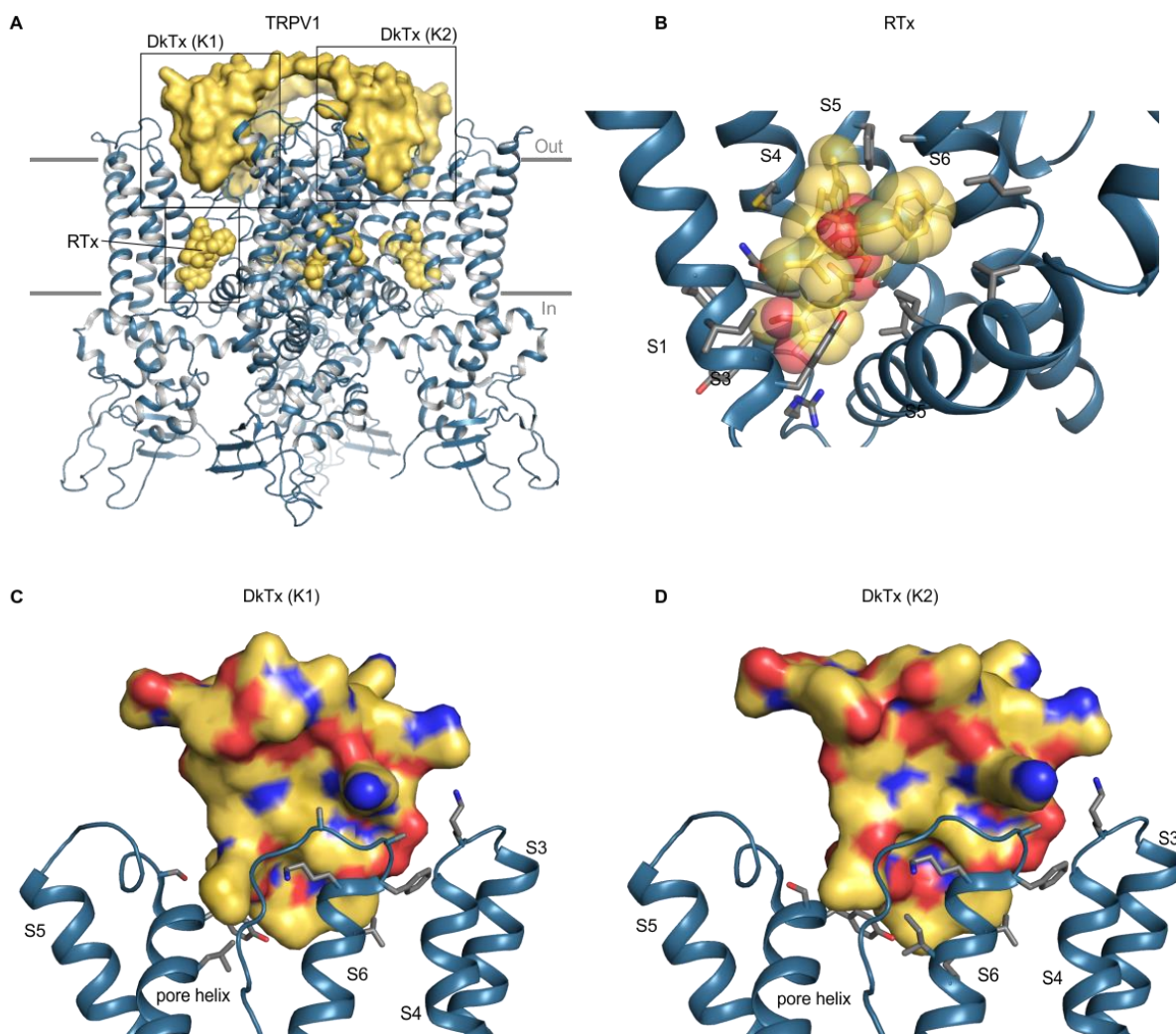
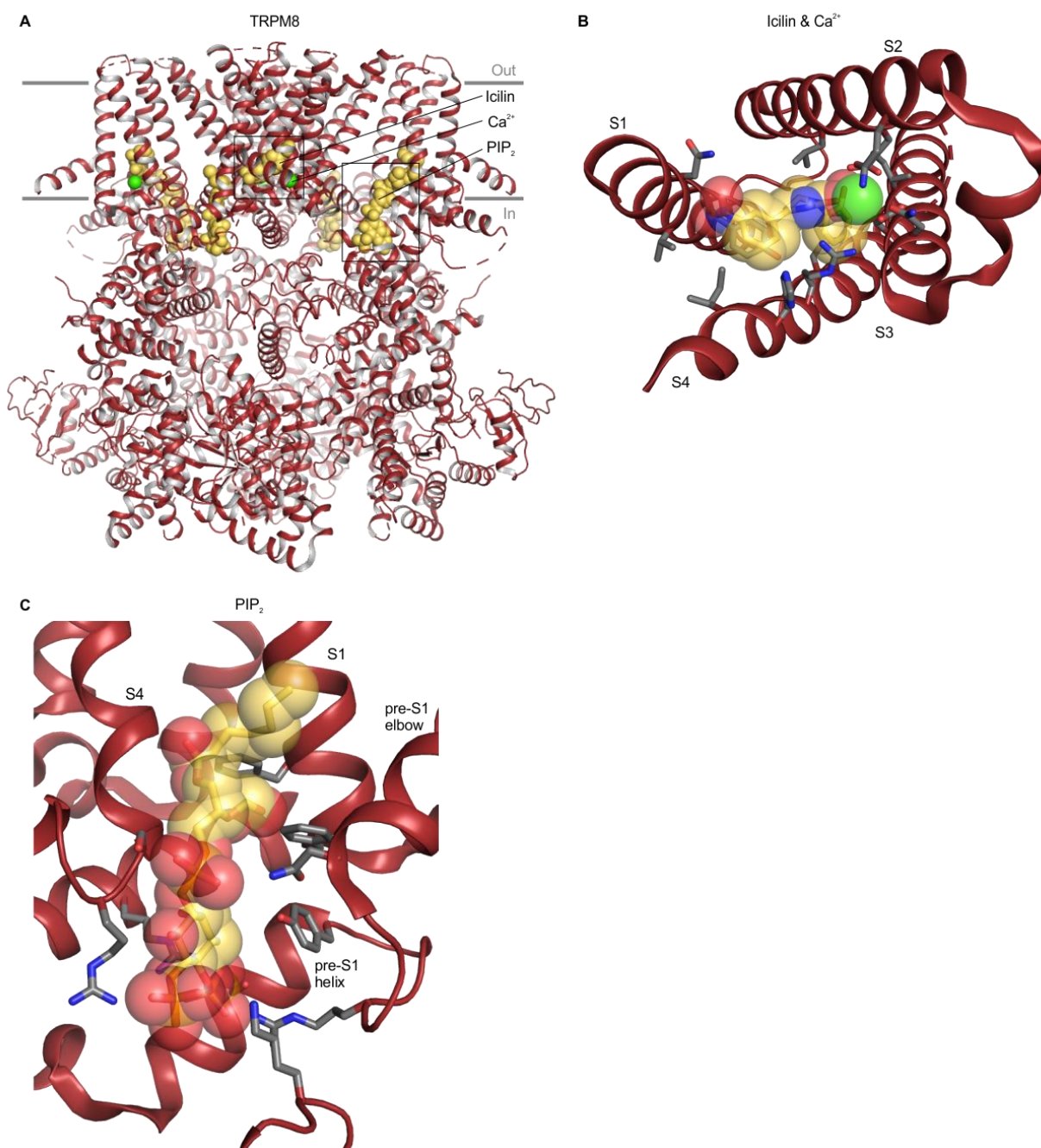


Figure 7. Structure of TRPV1 with RTx and DkTx bound.

(A) Structure of TRPV1 in nanodiscs with RTx and DkTx shown as yellow spheres and yellow surface, respectively (5irx). (B) Close up view of the RTx binding pocket with side chains colored by atom: carbon (gray), oxygen (red) and nitrogen (blue). (C,D) Close-up views of the DkTx binding surface showing either K1 or K2 knots, with linker omitted and side chain coloring as in B. Views are from the central pore axis looking out towards the lipid membrane. For clarity, helices without binding pocket residues have been hidden in panels B-D.



← **Figure 8. Structure of TRPM8 with icilin, Ca²⁺ and PIP₂ bound**

(A) Structure of TRPM8 with icilin, Ca²⁺ and PIP₂ bound (6nr3), with yellow spheres for ligands and green spheres for Ca²⁺. (B) Close-up view of the icilin and Ca²⁺ binding site from the intracellular side of the membrane with side chains colored by atom: carbon (gray), oxygen (red) and nitrogen (blue). The TRP helix has been removed for clarity. (C) Close-up views of the PIP₂ binding site, with side chain coloring as in B. For clarity, helices without binding pocket residues have been hidden in panels B and C.

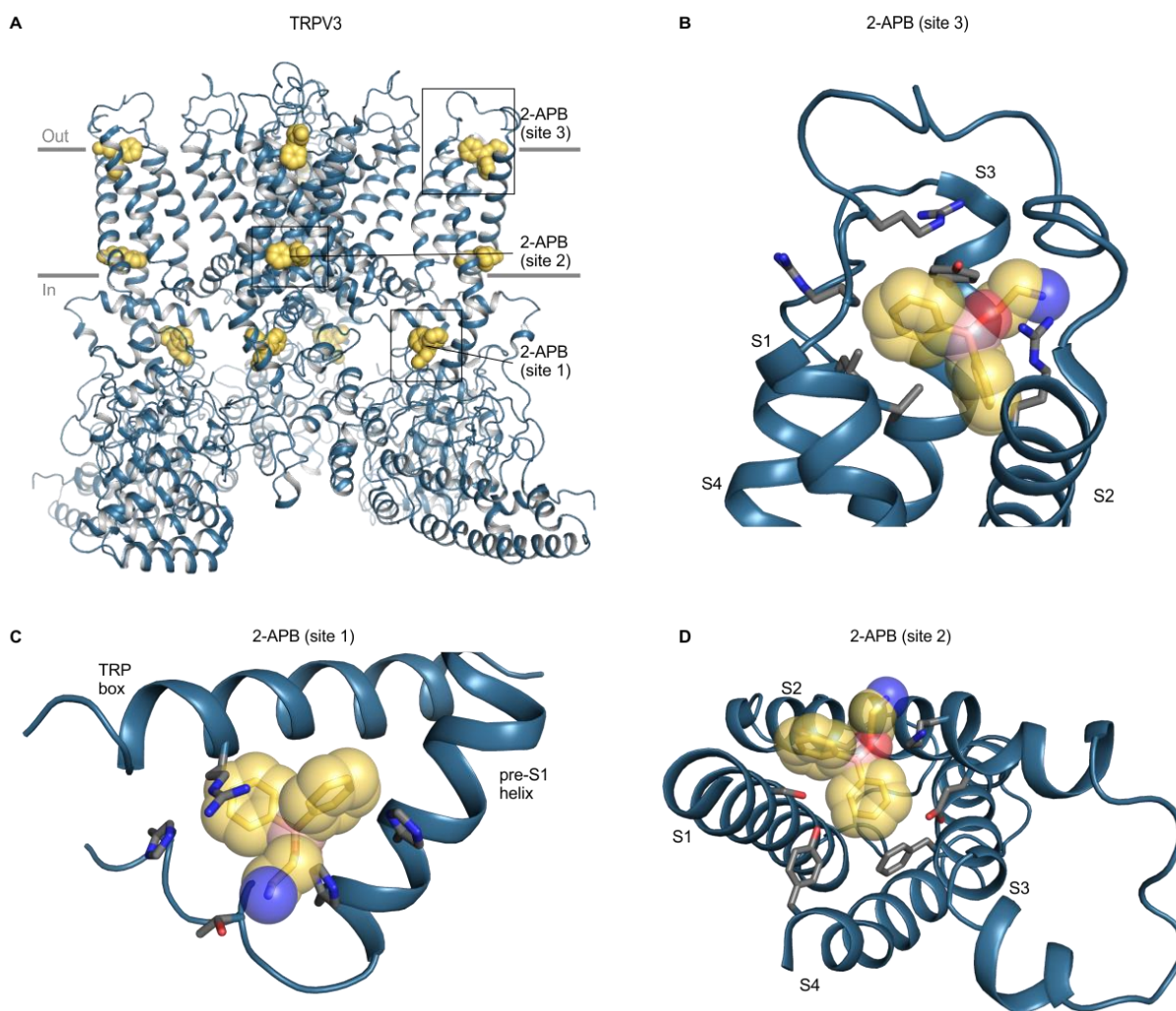
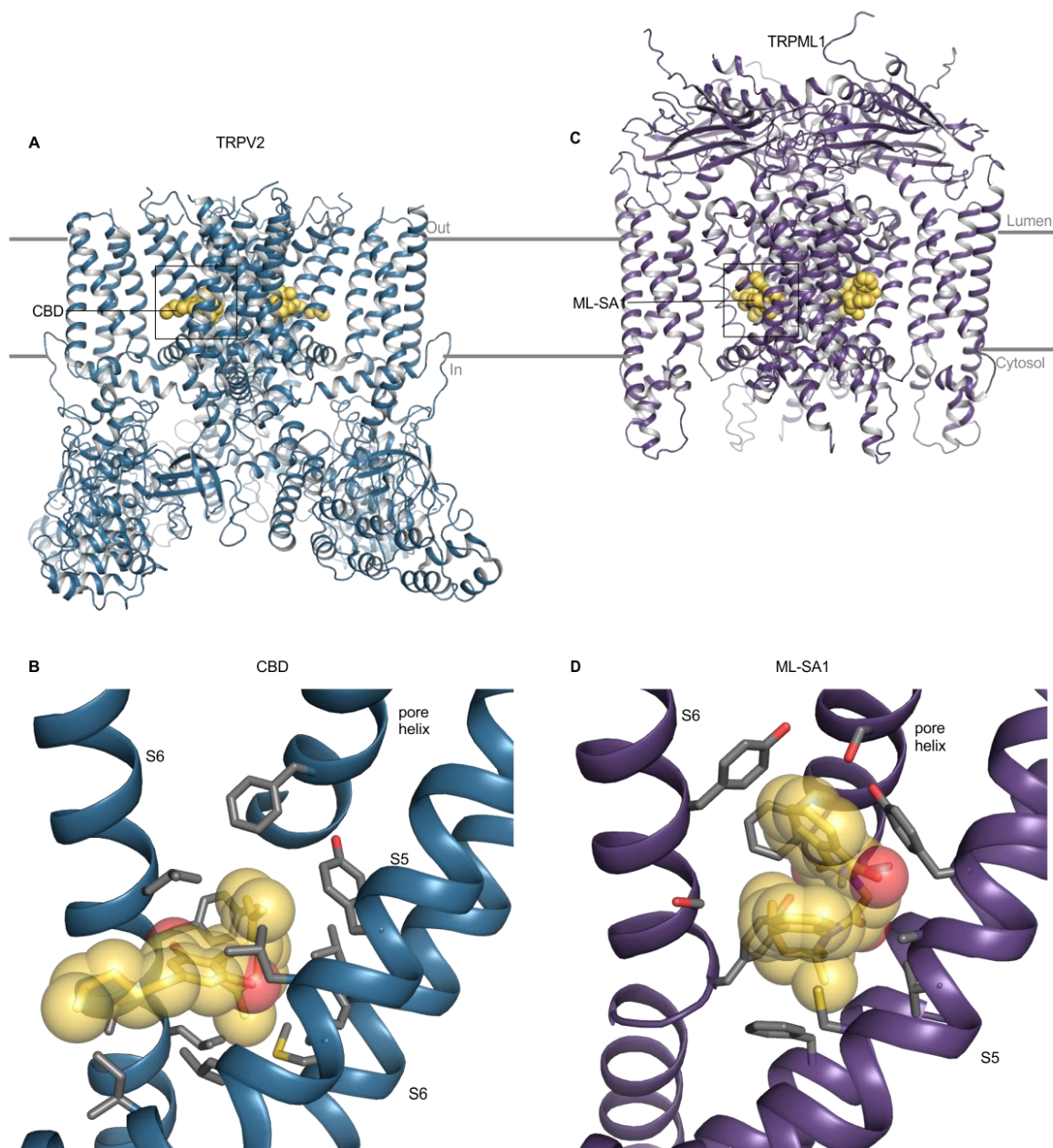


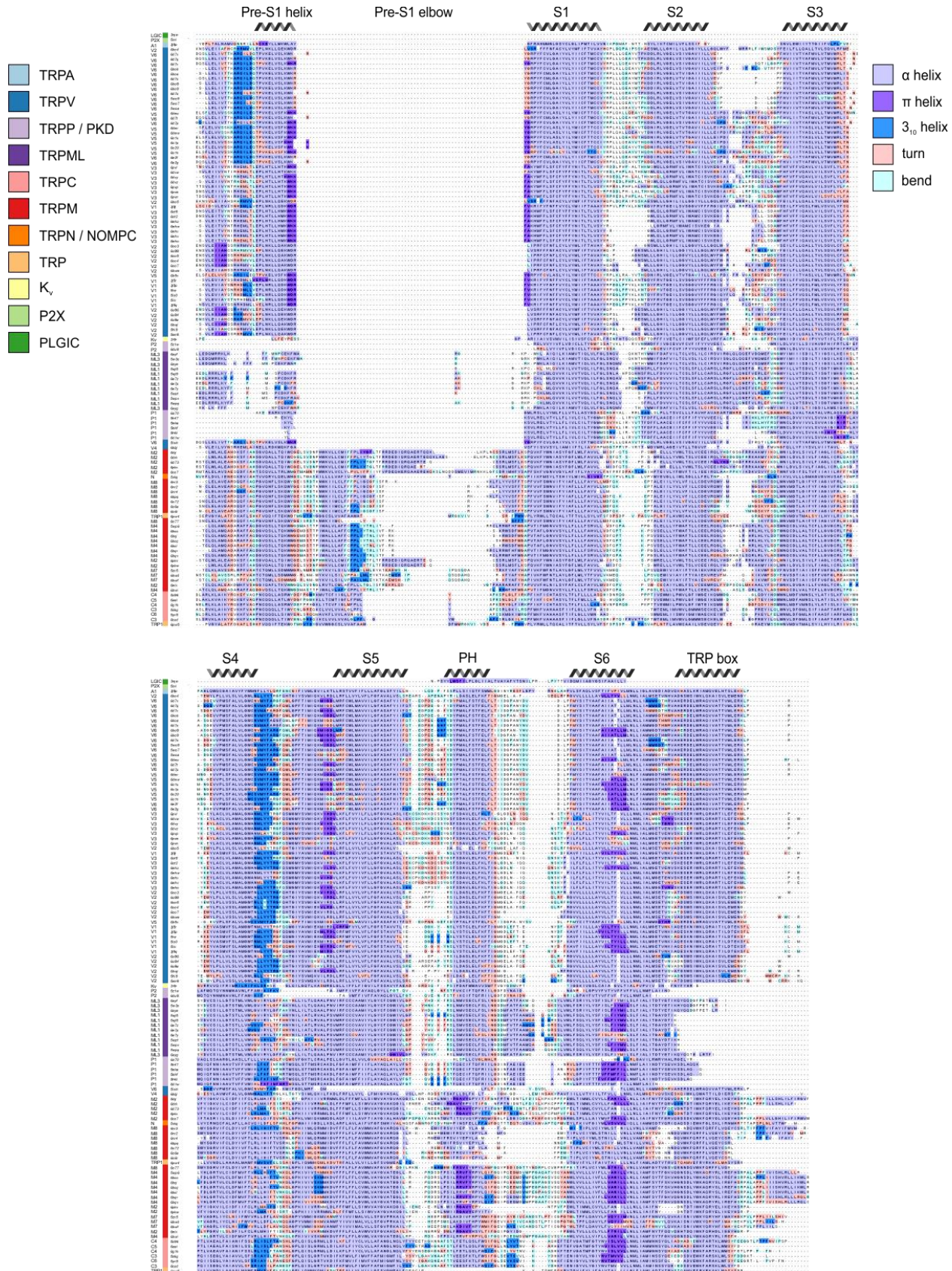
Figure 9. Structure of TRPV3 with 2-APB bound.

(A) Structure of 2-APB bound TRPV3 (6dvz), with ligands shown as yellow spheres. (B-D) Close-up views of the three 2-APB binding sites with side chains colored by atom: carbon (gray), oxygen (red) and nitrogen (blue). Boron atoms in 2-APB are colored in pink. Close-up in D is shown from the intracellular side of the membrane from same point of view as Figure 8B. For clarity, helices without binding pocket residues have been hidden in panels B-D.



← **Figure 9 – Figure Supplement 1. Ligand binding sites in TRPV2 and TRPML1.**

(A) Structure of TRPV2 with CBD bound (6u88), with ligands shown as yellow spheres. (B) Close-up view of the CBD binding site with side chains colored by atom: carbon (gray) and oxygen (red). For clarity, helices without binding pocket residues have been hidden. (C) Structure of TRPML1 with ML-SA1 bound (5wj9), with carbon (yellow) and oxygen (red). (D) Close-up view of the ML-SA1 binding site with side chains colored by atom: carbon (gray) and oxygen (red). For clarity, helices without binding pocket residues have been hidden. Panels B and D are from same point of view.



← **Figure 10. Alternate helical conformations with the TM segments of TRP channels.**

Structure-based sequence alignment, with residues colored based on secondary structure assigned by the dssp algorithm. Sequences are ordered based on hierarchical clustering from Figure 2. Segments, including TM helices and other regions identified in Figure 1F, are labeled based on α -helicity consensus. PH stands for pore helix.

Figure 10 – Source Data 1 **Data file for S6 radius and consecutive S6 π helices scatterplot**

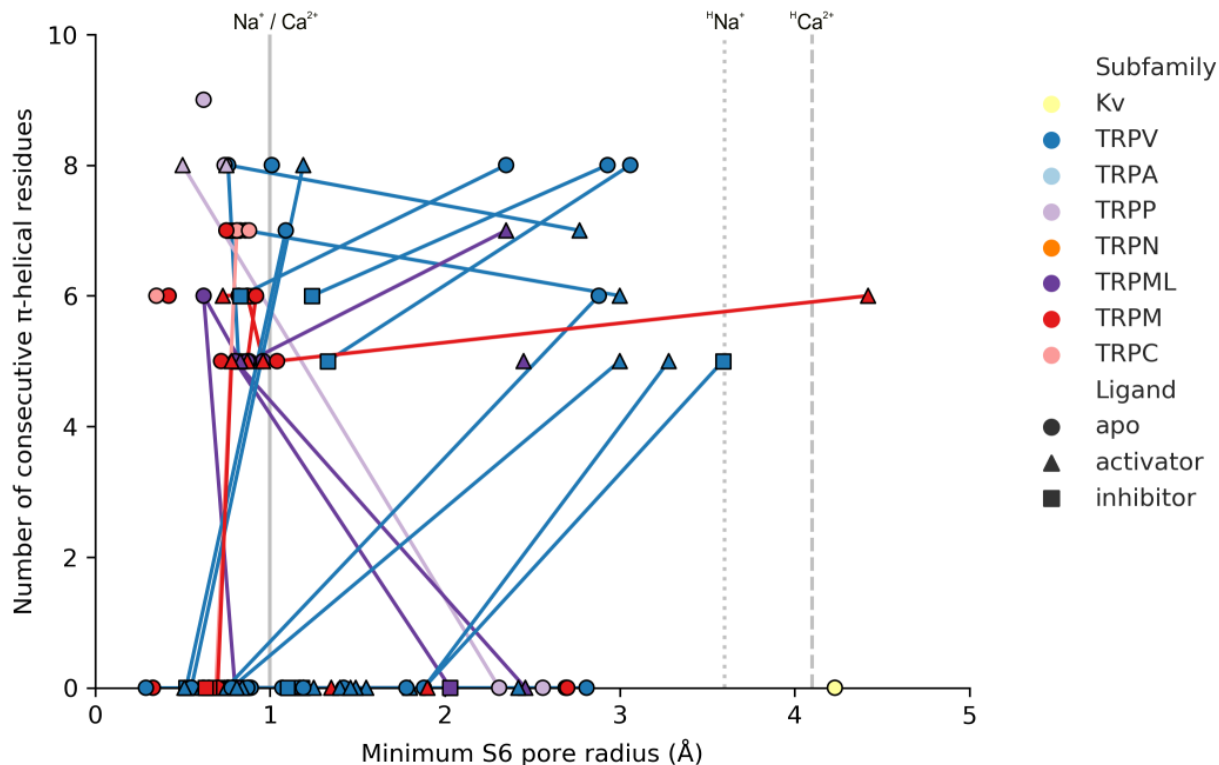


Figure 10 – Figure Supp. 1. Relationships between alternate helix conformations and the radius of the internal pore in TRP channels.

Plot of the number of consecutive residues in S6 that are identified as π -helical by the dssp algorithm against the minimal internal pore radius. Each marker represents one structure. Markers that represent the same channel determined under different conditions to obtain different conformations are connected with lines. Grey lines represent radii of dehydrated Na^+ and Ca^{2+} ions (solid), hydrated Na^+ (dotted, $^h\text{Na}^+$) and hydrated Ca^{2+} ions (dashed, $^h\text{Ca}^{2+}$).